D.Testa, L.Garzotti, C.Giroud, and JET-EFDA contributors

Assessment of the Calculation of the Radial Electric Field in JET Tokamak Plasmas

Assessment of the Calculation of the Radial Electric Field in JET Tokamak Plasmas

D.Testa[1], L.Garzotti[2], C.Giroud[3], and JET-EFDA contributors*

[1]*CRPP, Association EURATOM – Confédération Suisse, EPFL, Lausanne, Switzerland*
[2]*Consorzio RFX – Associazione EURATOM-ENEA sulla Fusione, I-35127 Padova, Italy*
[3]*Euratom – UKAEA Fusion Association, Culham Science Centre, Abingdon, UK*
*See appendix of J. Pamela et al., "Overview of JET results", in Proc of 19th IAEA Fusion EnergyConference, Lyon, 2002 (IAEA, Vienna, 2003)** Partner in the Trilateral Euregio Cluster (TEC)

ABSTRACT

The radial electric field E_r, and particularly its gradient, has been invoked by various theories and empirical models as a crucial parameter for determining the transition to high confinement regimes, such as the onset of an Internal Transport Barrier in the plasma core and of the H-mode pedestal at the plasma edge. Following a recent absolute calibration of the charge exchange diagnostic system, we have evaluated the uncertainty on the calculated E_r. Starting from the neoclassical moment approach of Hirshman and Sigmar, simple approximations have been used to reduce the full matrix calculation to a set of analytical formulas, adapted for the 2D toroidal geometry of JET to describe all collisionality regimes (banana, banana-plateau, Pfirsch-Schlüter), and to include a calculation of the error bars on E_r. Here we compare this analytical calculation with the results of the JETTO and NCLASS codes. Specifically, we assess how different approaches to treat numerically certain input plasma parameters for this calculation (ion density and effective charge profiles) can yield very different results for E_r. This is particularly clear for the plasma edge, where the contribution of the toroidal rotation velocity to E_r becomes small and comparable to the poloidal velocity and pressure components: hence uncertainties in the ion density profiles dominate the calculation of E_r. On the other hand, excluding such edge and core regions of the plasma (where the typical scale lengths become comparable to the ion poloidal Larmor radius), we find a striking similarity in the shape of E_r in L-mode and ITB plasmas, and we demonstrate the role of prompt fast ion losses when comparing H-mode plasmas with forward and reversed ion ∇B-drift direction. Our analysis points clearly to the need for routine measurements of the poloidal velocity and E_r if detailed comparison with code predictions and empirical scaling laws are to be made for studies and modelling of improved confinement regimes.

1. INTRODUCTION.

The radial electric field E_r, and particularly its gradient ∇E_r, has been invoked by various theories and empirical models as a crucial parameter for determining the transition to high confinement regimes, such as the onset of an Internal Transport Barrier (ITBs) in the plasma core [1,2] and of the H-mode pedestal at the plasma edge [3]. Various classic examples of these studies are given in the review papers indicated in Ref.[4]. Hence, it is crucial to obtain detailed and accurate measurements of the time-and-space evolution of $E_r(r,t)$, with an assessment of their uncertainty, for validating such model calculations, if reliable predictions of improved confinement regimes are to be made. The radial electric field is not directly measured in the JET tokamak [5] at the present time, and for a long time it has been routinely computed mixing the contribution of different ion species: the measured carbon toroidal rotation, the computed deuterium pressure gradient (from the measured ion temperature and computed deuterium density), and the computed neoclassical mass-averaged ion poloidal velocity. This approach contradicts the fact that $E_r(r,t)$ is an overall property of the plasma, common to all ion species, hence it should be computed independently for the main and the impurity ions, to check the consistency of the numerical results. Some earlier measurements of the

edge radial electric field were indeed performed in JET to assess its importance in the L-to-H mode transition [6], but have not been routinely repeated since the hardware and views were changed. Based on the neoclassical moment approach of Hirshman and Sigmar [7], an analytical formulation was initially developed in Ref.[8] to reduce the full matrix calculation to a set of readily tractable equations. The validity of this approach for the JET tokamak was verified by comparing the inferred deuterium toroidal rotation velocity with that obtained from the Doppler shift in the frequency of radially localised magneto-hydrodynamic modes [9]. This analytical formulation was extended to all collisionality regimes (banana, banana-plateau and Pfirsch-Schlüter) to include the 2D geometry of the JET flux surfaces, averaging over the ion orbit width. Furthermore, following up from a recent absolute calibration of the JET Charge eXchange (CX) diagnostic system [10], we have also included an analytic calculation of the error bar on the 3D radial electric field profile $E_r(r,t)$.

In this paper we compare the results of this analytical calculation with the results of the JETTO [11] and NCLASS [12] codes for various typical JET plasma scenarios: L-mode, ELMy and ELM-free H-modes (with normal and reversed ion ∇B-drift direction), and ITB with a deeply and moderately reversed safety factor profile. In particular, we assess how different approaches to treat numerically certain input plasma parameters for this calculation (essentially the ion density and effective charge profiles) yield rather different results for E_r. This is particularly clear for the plasma edge, where the contribution of the toroidal rotation velocity to E_r becomes small and comparable to the poloidal velocity and pressure components, with significant implications for testing theories that associate the L-H transition to the edge values of E_r and ∇E_r.

This paper is organized as follows. Section 2 gives a rapid overview of the core CX system in JET, with particular focus to its absolute calibration, and Section 3 briefly describes the JETTO and NCLASS codes. In Section 4 we overview the neoclassical moment approach of Ref.[7] and how we have adapted and extended it to the specific JET case following up from the methods described in [8,9]. Section 5 presents the comparison between various model calculations for the ion poloidal velocity, whose role is particularly important in determining the radial electric field where steep pressure gradients exists, such as at the plasma edge (L-to-H mode transition) and towards mid-radius (ITB formation). In Section 6 we present in details the error analysis we have adopted here, focusing specifically on the contribution of the uncertainty in the raw data when taking their gradients, and on the use of different numerical approaches to fit, inter- and extra-polate the "raw" input data. Section 7 presents the comparison between the JETTO and NCLASS code calculations and the results of our analytical formulation for a reference JET plasma undergoing the L-to-H-mode transition, to estimate the differences in the resulting $E_r(r,t)$ due to the different choices for numerical treatment of the input data profiles, and compare these differences with the uncertainties in $E_r(r,t)$. Sections 8 and 9 present the results of our analysis for the two groups of JET operating regimes we have analysed here, the L-to-H mode transition in the conventional tokamak scenario (with a monotonic safety factor profile) and the ITB formation in the advanced tokamak scenario (non-monotonic safety factor profile), respectively. Finally, in Section 10 we discuss these results and present our conclusions.

2. OVERVIEW OF THE CORE CX SYSTEM AND ITS ABSOLUTE CALIBRATION.

In this paper, the charge-exchange diagnostic provides the measurements of the ion temperature T_i, of the carbon toroidal rotation $V_{\phi C}$ and of the carbon density n_C profiles over the radial interval $2.9 < R(m) < 3.8$, where R is the plasma major radius along the midplane. It is important for the scope of this paper to briefly discuss the issue of statistical and systematic error on these measurements, but the issues related to the spatial resolution of the measurements will however not be considered here. A complete description of the method used for the absolute calibration of the JET core CX diagnostic and its results is given in [10]. The ion temperature and toroidal velocity are determined from the Doppler broadening and the Doppler shift of the C^{6+} charge-exchange line (5290.54Å), respectively. The error on $T_i(r,t)$ is only of statistical nature, being related to the result of the multi-Gaussian fit used to analyse the features of the C^{6+} line. On the other hand, the error in $V_{\phi C}(r,t)$ has two components: a statistical one resulting from the multi-Gaussian fit and a systematic one linked to the uncertainty in the angle between the line of sight and the toroidal direction at the intersection volume between the neutral beam injection (NBI) trajectory and the line of sight. The carbon concentration at this position is calculated from the measured emissivity of the CX line using knowledge of the CX cross-section and the fast neutral density in this observation volume due to the injected beam ions, deduced from a beam attenuation code. The error on $n_C(r,t)$ is hence the combination of a statistical error, related to the measured emissivity of the CX line as determined from the spectral fit, and of a systematic error. For the latter, we do not consider the uncertainties of the fast neutral densities in the intersection volume as determined by the beam attenuation code, but only the uncertainty in the position of this volume. Overall, following the detailed calibration work presented in Ref.[10], it was determined that the absolute error σ is $\sigma(n_C) \approx 0.3 n_C$, $\sigma(V_{\phi C}) \approx 0.15 V_{\phi C}$ and $\sigma(T_i) \approx 0.05 T_i$.

3. OVERVIEW OF THE JETTO AND NCLASS CODES.

JETTO [11] is a 1.5 dimensional transport code solving equations for the plasma current, the ion density, the electron and ion temperature and the ion toroidal velocity. In addition JETTO uses the effective charge $Z_{EFF} = \sum_i n_i Z_i^2 / n_e$ and an average charge state for impurities to estimate the electron density and the impurity concentration. The toroidal velocity appearing in JETTO equations is thus a quantity mass density averaged over the main and impurity ion species in the plasma. JETTO has been coupled to NCLASS [12] for the computation of neoclassical transport coefficients. NCLASS follows the formulation of Hirshman and Sigmar [7] and solves a matrix for plasma flows within and across magnetic surfaces derived from the parallel and radial force balances for plasmas with multiple ion species. A very important difference in the treatment of impurities between JETTO and NCLASS is that, as indicated previously, JETTO uses an average charge state for impurities, while NCLASS treats each impurity charge state separately. To combine the two codes it has been chosen to split the effective charge in JETTO between neighbouring states for input to NCLASS and then collapse the resulting NCLASS output to a set of effective quantities that conserve the

sum over the charge states. The advantage of using JETTO and NCLASS together is that one can then take into account realistic plasma equilibria and geometries and avoid many of the approximations that are used to derive simple analytic expressions for neoclassical quantities.

4. ANALYTIC TREATMENT OF NEOCLASSICAL MOMENT APPROACH.

The radial electric field $E_r(r,t)$ is computed from the force balance equation

$$E_r(r, t) = \frac{1}{Zen(r, t)} \frac{dp(r, t)}{dr} + sign(B_\phi)V_\theta(r, t)/B_\phi(r, t)/-V_\phi(r, t)B_\theta(r, t), \qquad (1)$$

where the pressure (p), density (n), charge (Ze), atomic mass (Am_p) and rotation velocities (toroidal, V_ϕ, and poloidal, V_θ) are all species dependent quantities, B_ϕ and B_θ are the toroidal and poloidal magnetic field, respectively, and r is the radial coordinate along the plasma minor radius. Note that the toroidal magnetic field is a signed quantity, negative in the standard JET operating configuration (counter-clockwise when viewed from above the plasma midplane). Since E_r is an overall property common to all the ion plasma species, using in Eq.(1) quantities for the main (deuterium, D) and the impurity (carbon, C) ion species must give the same result, within the error bar of the measurement and calculation. The condition $E_{rC} \approx E_{rD}$ has been verified for all the discharges analysed here, giving $2 \times |E_{rD}-E_{rC}|/|E_{rD}+E_{rC}|<15\%$, comparable to the uncertainty in the calculation of E_r (see Section 5). This condition is a basic consistency check of the calculation: if $E_{rC} \neq E_{rD}$ within the error bars, then there must for sure be an error in the calculation. The condition $E_{rC} \approx E_{rD}$ is not a standard result, in the sense that by using different ion density and Z_{EFF} profiles one can easily get $E_{rC} \neq E_{rD}$, i.e. with the difference larger than the error bar on the calculated radial electric field. To evaluate Eq.1, we have used the CX measurements of the carbon density n_C, of the ion temperature $T_C=T_D=T_i$, of the carbon toroidal velocity $V_{\phi C}$, and of the magnetic field, using the Motional Stark Effect (MSE) diagnostic to measure the safety factor profile q(r), hence evaluate B_θ.

   In this work we start from the neoclassical moment approach of Hirshman and Sigmar [7], which is derived for plasmas composed of electrons, one main ion species (deuterium) and only one impurity ion species, carbon in our case. This approach involves solving matrixes for plasma flows within and across magnetic surfaces derived from the parallel and radial force balances for plasmas with two ion species, which requires the use of heavy computational tools. An analytical approach to compute the various neoclassical coefficients determining the deuterium toroidal velocity $V_{\phi D}$ and the carbon and deuterium poloidal velocities $V_{\theta C}$ and $V_{\theta D}$ has been developed by various authors using different simplifications for the plasma geometry and the physics terms to be included. The clear advantage of such analytic approaches is that they make it possible to investigate in greater details and with much more "experimental" control certain aspects of the full-matrix neoclassical formulation, without having to rely on heavy and often cumbersome computational tools, which may become somewhat difficult to interpret and understand at times.

Following Ref.[7] and starting from the general results of Ref.[8], the differential toroidal rotation velocity between the deuterium (computed) and carbon (measured) $\Delta V_\phi = V_{\phi D} - V_{\phi C}$ is given by:

$$\Delta V_\phi = -\,sign(B_\phi)\,\frac{\upsilon_{thD}\rho_{\theta D}}{4L_{TD}}\left[K_2\left(1 - \frac{3B_\phi^2}{<B^2>}\right) - \frac{L_{TD}}{L_{pD}}\left(1 - \frac{Z_D T_C}{Z_C T_D}\frac{L_{TD}}{L_{pC}}\right)\left(1 - \frac{B_\phi^2}{<B^2>}\right)\right], \quad (2)$$

where the (r,t) dependency has been dropped for clarity. Here v_{th} and ρ_θ are the ion thermal speed and poloidal gyroradius, respectively, B is the total magnetic field, taken as $B=(B_\phi^2+B_\theta^2)^{1/2}$ (thus neglecting for simplicity the diamagnetic, radial and vertical components), and the brackets $<>$ indicate flux surface averaging. The pressure scale length L_p is related to the temperature and density scale lengths L_T and L_n by $1/L_p=1/L_T+1/L_n$. Here $1/L_X=d(\ln X)/dr$, thus the scale length is negative for a quantity that decreases with the minor radius. We wish to point out here that the use of the term $sign(B_\phi)$ in Eq.(2) and below allows us to apply the same formulation for all pulses with the same plasma helicity, i.e. $sign(B_\phi I_p)$=constant, which is the usual JET operating scenario. A more complex analytic formulation can also be derived for a non-constant plasma helicity, i.e. when the directions of the plasma current and toroidal magnetic field are independently reversed. Equation (2) has been obtained by neglecting the electron contribution to the viscous and friction forces and the impurity viscous force compared to the friction force between the impurity and the main ion species. Defining the impurity strength parameter $\alpha=(n_C Z_C^2/n_D Z_D^2)$, the parameter K_2 is given as function of α and $\beta=(6.75A_D/A_C)^2/[7.5+(2\alpha A_C/A_D)^{1/2}]$ as:

$$K_2 = (\mu_{00}\mu_{11} - \mu_{01}^2)/D, \quad (3a)$$

$$D = \mu_{00}\left[\mu_{11} + \sqrt{2} + \alpha(1-\beta) - \mu_{01}^2\right]. \quad (3b)$$

The coefficients μ_{ij} entering the calculation of K_2 are those for the main ion species, but these are species-dependent quantities (hence the superscript s below) given by the general relation:

$$\mu_{ij,\,s} = \frac{G\mu_{ij,\,s}^{BA}}{(1 + 2.92v_*\mu_{ij,\,s}^{BA}/\mu_{ij,\,s}^{PL})(1 + \mu_{ij,\,s}^{PL}/\mu_{ijs}^{PS}/\omega_{ts}/\tau_s/6)}. \quad (4)$$

This formulation provides a clear and simple analytic format for the transition between the various collisionality regimes, indicated by the acronyms BA (banana), PL (plateau) and Pfirsch-Schlüter (PS), using a Padé approximation of the different mij coefficients as function of the normalised ion collision/bounce frequency v^*. Using $\mu_{01}=2.5\mu_{00}-k_{01}$, and noting that Eq.(4) also applies to k_{01}, the μ_{00}, μ_{11} and k_{01} coefficients for the main ion species (here deuterium) are given by:

$$\mu_{00,\,D}^{BA} = \frac{0.53 + \alpha}{S_D^{3/2}} \;,\; \mu_{00,\,D}^{PL} = 1.77 \;,\; \mu_{00,\,D}^{PS} = \frac{3.02 + 4.25\alpha}{2.23 + \alpha(5.32 + 2.4\alpha)},$$

$$(5a)$$

$$\mu^{BA}_{11,D} = \frac{1.39 + 3.25\alpha}{S^{3/2}_D} \quad , \mu^{PL}_{11,D} = 5.76 \quad , \mu^{PS}_{11,D} = \frac{15.18 + 26.97\alpha}{2.23 + \alpha(5.32 + 2.4\alpha)} \, , \tag{5b}$$

$$k^{BA}_{01,D} = \frac{0.71 + \alpha}{S^{3/2}_D} \quad , k^{PL}_{01,D} = 5.32 \quad , k^{PS}_{01,D} = \frac{12.43 + 20.13\alpha}{2.23 + \alpha(5.32 + 2.4\alpha)} \, , \tag{5c}$$

The μ_{ij} coefficients for the impurity ion species (here carbon) and electrons can be obtained from those for the main ion species with the substitution $\alpha \to 1/\alpha$ for the impurities and $\alpha \to Z_{EFF}$ for the electrons. In Eq.(4) $G=F_{TRAP}/F_{CIRC}$ is the trapped/circulating ion fraction, $F_{TRAP} \approx \sqrt{\varepsilon}(1.46-0.46\varepsilon)$ in the large aspect ratio limit ($F_{TRAP}+F_{CIRC}=1$), where $\varepsilon=r/(R_0+_r)$ is the normalised local minor radius (R_0 being the position of the magnetic axis), and

$$X_s = \left[\frac{1}{n_S Z_S e} \frac{dp_S}{dr} - V_{\phi S} B_\theta \right] , \tag{6a}$$

$$S_s = 1 - \frac{4\pi^2 A_S}{Z_S} \rho_{\theta s} \frac{X_S}{\upsilon_{ths} B_\theta} \left| \frac{d\,log(RB_\theta)}{dr} - \frac{d\,log(X_S)}{dr} \right| , \tag{6b}$$

$$\tau_s = 6.6 \times 10^{-2} \frac{\sqrt{A_S T_i^3}}{n_e Z_s^2 log\Lambda_s} \, , \quad log\Lambda_s = 17.3 - log\,(n_s) + 1.5log\,(T_i) - 3log\,(Z_s), \tag{6c}$$

$$v_* = \frac{\omega_{tD}}{2\tau_D \upsilon_{thD}^2} \left\langle \left(\frac{B}{\nabla B} \right)^2 \right\rangle \left[1 + \alpha \left(2.83 + \alpha \sqrt{\frac{A_C}{A_D}} \right) \right] \frac{G\,/\,1.46}{\left[1 + 7\,(1 - F_{CIRC})^2 \right]} \tag{6d}$$

In Eq.4 $S \approx [0.8\text{-}1.2]$ is the orbit squeezing parameter [13], which applies only to the BA regime, $\omega_t = v_{th}/q/R$ is the ion thermal transit time frequency, τ is the ion slowing-down time and v_* has been generalised here to include its trapped particle scaling [14] and all ion/electron, ion/ion and ion/impurity collisions; $R=R_0+r$ is the plasma major radius, and the numerical factors in Eq.6(c) are evaluated for the temperature in units of [keV] and the density in units of $[10^{20}\text{m}^{-3}]$. Note that the definition of v^* adopted here is rather different from the most common one, $v_{*X}=qR\varepsilon^{-3/2}/\tau_D/v_{thD}$, but the two correspond in the large aspect ratio limit when only ion-electron collisions are included.

Starting from Ref.[8], the neoclassical formulation of V_θ depends on the collisionality parameter K_1 and on the temperature and pressure scale lengths as (ρ_ϕ being the ion toroidal gyroradius):

$$K_1 = \mu_{01} \left[\hat{2} + \alpha\,(1 - \beta) \right] / D \, , \tag{7}$$

$$V_{\theta C} = -\,sign\,(B_\phi)\,K_1 \frac{\upsilon_{thD}\,\rho_{\phi D}}{2L_{TD}} \frac{|BB_\theta|}{<B^2>} \, , \tag{8a}$$

$$V_{\theta C} = -\,sign\,(B_\phi)\,K_1\,\frac{\upsilon_{thD}\,\rho_{\phi D}}{2L_{TD}}\left[\left(K_1 + \frac{3K_2}{2}\right) - \frac{L_{TD}}{L_{pD}}\left(1 - \frac{Z_D\,T_C}{Z_D\,T_C}\,\frac{L_{pD}}{L_{pC}}\right)\right]\frac{|BB_\phi|}{<B^2>}\ .\ \text{(8b)}$$

Alternatively, by neglecting the contribution of the ion and impurity pressure scale lengths to the poloidal velocity, a different approach can be used to derive the neoclassical coefficient k_{NEO}, so that $V_\theta \approx k_{NEO}\nabla T$, as recently introduced by Tokar in Ref.[15]. Here a Padé approximation of k_{NEO} as function of ν_{*X} was considered. Hence, alternative expressions for $V_{\theta C}$ and $V_{\theta D}$ were obtained as:

$$V_{\theta S}^{(\nabla T)} = -\,sign\,(B_\phi)\,k_S{}^{NEO}\ \frac{\upsilon_{ths}\rho_{\phi S}}{2L_{TS}}\ ,\tag{9a}$$

$$k_s{}^{NEO} = 1.83\,\frac{0.061 + v_{*X}^s\,\varepsilon^{3/2}}{0.222 + v_{*X}^s\,\varepsilon^{3/2}}\,\frac{v_{*X}^s - 0.703}{v_{*X}^s + 0.302}\ .\tag{9b}$$

The neoclassical theory used to derive Eqs.2-9(b) is expected to break-down when the scale lengths are much shorter than the main ion poloidal gyroradius, L's$\ll\rho_{\theta D}$. This typically occurs in the high magnetic shear region at the plasma edge or in the core of plasmas with a deeply reversed q-profile, where $\rho_{\theta D}\approx$L's even for flat (density, temperature) profiles since $B_\theta\rightarrow 0$ over a large region (i.e., not only on the magnetic axis). A practical spatial limit for the validity of the neoclassical theory in the plasma core is then to take the ion banana orbit width, $\delta_{BAN}\approx q\rho_\theta/\sqrt{\varepsilon}$, and linearly extrapolate the results towards the magnetic axis for all points $0<r\leq\delta_{BAN}$.

The validity of Eq.(2) was first experimentally verified on the Doublet III-D tokamak (DIII-D) [16]. Direct measurements of the ion toroidal rotation velocities were performed using CX recombination spectroscopy of the main ion species, He^{2+}, and of the impurity ion species C^{6+} and B^{5+} in DIII-D helium plasmas with a monotonic q-profile [17]. The right hand side of Eq.(2) was computed from the measured profiles and showed a very good agreement with the measurement of ΔV_ϕ, the only significant discrepancy arising in the high magnetic shear region at the plasma edge. The validity of this approach for the JET tokamak was successfully verified in Ref.[9] by comparing the inferred deuterium toroidal rotation velocity with that obtained from the Doppler shift in the frequency of radially localised magneto-hydrodynamic modes.

It is important to note here that for comparison with codes such as JETTO and NCLASS, flux-surface averaging of Er, V_ϕ and V_θ is needed. This operation can be treated analytically (but for the flux surface expansion towards the X-point) using the original straight-field line approximation of Merezkhin [18], adapted here to include the plasma elongation and triangularity, following from the derivation presented in Ref.[19]. This method is valid up to x$\approx$0.95 for low-β_θ plasmas in the limit of low edge triangularity δ_{95}, such that δ_{95}/κ_{95}=O(ε(x)) and β_θ=O($\sqrt{\varepsilon}$(x)), where x=$\sqrt{\psi_N}$ is

our radial coordinate, ψ_N being the normalised poloidal flux The validity of this analytical treatment of the flux-surface averaging is checked by comparing its results with the JETTO ones for the flux-surface averaged radial profiles of n_e, T_e, T_i and B_θ. The transformation between the "real toroidal" and the "analytic circular" flux-surfaces is obtained as $(R,Z) \rightarrow [R_0 + \Delta_{SHAF}(x), J(x)r(x)]$. Here the Jacobian $J(x)$ of the transformation between a "true toroidal" flux surface and its geometrical approximation using an ellipse distorted by triangularity, with the centre displaced by the Shafranov shift Δ_{SHAF} is $J(x) = [1 + \kappa^2(x)]^{1/2}[1 + 2\delta(x)/\pi]/\sqrt{2}$. Hence, flux-surface averaging of a quantity X whose profile is a function of R is obtained using the geometrical factor $J^2/(2J^2-1)^{1/2}$, so that $<X> = X*[J^2/(2J^2-1)^{1/2}]$. All data presented in the following sections are to be considered as flux-surface averaged values.

A second point to discuss here is the radial averaging of $E_r(x,t)$ over the ion orbit width, which is not considered in JETTO nor NCLASS. Following from the analysis of Ref.[20], in the usual case of a monotonic q-profile the trapped ions have all banana orbits with guiding centre on a given flux-surface: the banana orbit width is $\delta_{BAN} \approx q\rho_\theta/\sqrt{\varepsilon} \sim 3 \div 10$cm. However, for the case of a non-monotonic q-profile, an important fraction of the trapped ion orbits is represented by non-standard potato ones, whose width much exceed that of the typical banana orbits. Continuing and extending the work of Ref.[20], the width of a potato orbit can be analytically estimated as:

$$\delta_{POT} \approx R_0 \left(\frac{2q\upsilon_\perp}{R_0 \Omega_\phi} \right)^{2/3} = R_0 \left(\frac{4q\,\rho_\theta}{R_0} \right)^{2/3} \approx \frac{\varepsilon^{5/6}}{q} \left(\frac{16R_0}{\rho_\theta} \right)^{1/3} \delta_{BAN} \, , \tag{10}$$

where $v_\perp = \sqrt{2}v_{th}$ is the ion velocity perpendicular to the toroidal magnetic field, $\Omega_\phi = ZeB_\phi/Am_pc$ is the ion cyclotron frequency, and typically we have that $\delta_{POT} \approx 20(\varepsilon/q)\delta_{BAN}$ for $\delta_{BAN} > r$. To obtain an analytic treatment of the averaging over the ion orbit width, we have considered that all banana (and potato) orbits have the same width for ions whose guiding centre lies on a given flux-surface, hence neglecting the formal and very complex averaging over the exact ion velocity distribution function. Again following up Ref.[20], we have empirically estimated the potato/banana orbit fraction as:

$$\frac{F_{POT}}{F_{BAN}} \approx q_{MIN} \frac{|\sqrt{\varepsilon} - s_0|}{\sqrt{\varepsilon} + |s|} \frac{|q(r = \delta_{BAN}) - q_{MIN}|}{q(x = 0.95) - q_{MIN}} \, q \, (r = \delta_{BAN}) \, , \tag{11a}$$

$$F_{POT} + F_{BAN} \approx 2 \frac{|q_{MIN} - q \, (r = \delta_{BAN})|}{|q_{MIN} - q \, (r = \delta_{BAN})|} F_{TRAP} \, , \tag{11b}$$

$$\delta_{ORB} = \frac{F_{POT}\delta_{POT} + F_{BAN}\delta_{BAN}}{F_{POT} + F_{BAN}} \, , \tag{11c}$$

where q_{MIN} is the minimum in q(x), $s(x) = (r/q)(dq/dr)$ is the local magnetic shear (s_0 being the

8

value on-axis), and δ_{ORB} is the effective ion orbit width used for the radial averaging of $E_r(x,t)$ and its components. Note also that $F_{POT}+F_{BAN}=F_{TRAP}$ for a monotonic q-profile, where $q_{MIN}\approx q(r=\delta_{BAN})$.

5. EVALUATION OF THE ION POLOIDAL VELOCITY.

The radial electric field $E_r(x,t)$ given by the force balance equation, Eq.(1), contains the contribution of the toroidal ($V_\phi \times B_\theta$), poloidal ($V_\theta \times B_\phi$) and pressure gradient ($\nabla p/neZ$) components. The toroidal component is typically the dominant one since $|V_\theta/V_\phi|\approx o(|B_\theta/B_\phi|)$ and, moreover, the neoclassical poloidal and pressure gradient components often almost cancel out each other, leaving a resulting negligible net contribution to $E_r(x,t)$. However, this is not always the case towards the plasma edge, typically for x>0.9, where we often find that $|V_\theta/V_\phi|\approx O(|B_\theta/B_\phi|)$ because of the large reduction in the toroidal velocity due to a much smaller momentum input, and similarly may not be the case if $V_\theta(x,t)$ is anomalous (i.e. non-neoclassical), for instance at the ITB location. The carbon poloidal rotation velocity profile $V_{\theta C}(x,t)$ is indeed directly measured in many machines over the entire plasma cross-section, see as examples the results of Ref.[17], but this is not yet the routine case in JET due to certain difficulties with the present diagnostic setup, and indeed a new diagnostic system is currently being installed to correct these problems. In the following we have therefore decided to use the neoclassical value of $V_\theta(x,t)$. Hence, it is paramount to assess such neoclassical calculations, using the complete NCLASS formulation in comparison with the simplified analytical treatments provided by Eqs.8(a), 8(b) and/or Eqs.9(a), 9(b).

Figures 1(a) and 1(b) show the flux-surface averaged $<V_{\theta C}>$ and $<V_{\theta D}>$ calculated over the entire plasma cross-section using the same JETTO input profiles (with no orbit width averaging) at two time points during the L-mode and H-mode phase, respectively. We notice that the V_θ calculated using NCLASS and Eqs.8 (a), 8 (b) are similar to each other in the L- and H-mode phase, with only small differences in the plasma core, for $x=\sqrt{\psi_N}<0.2$, and at the plasma edge, for x>0.9, where $<V_{\theta C}>$ from NCLASS is large and negative, particularly in the H-mode phase. The differences for x>0.9 cannot be related exclusively to the treatment of the edge flux-surface geometry, and are thus indicative of further terms which are not properly captured by the analytic treatment of Eqs.8(a), 8(b). Further differences also arise when considering the various methods for inter/extrapolating the input data, as described in Section 7. Figure 1(b) also shows that the calculated $<V_{\theta D}^{\nabla T}>=<k_{NEO,D}\nabla T>$ is very different from the other two, notably in its sign. This difference is particularly significant in the H-mode phase (and similarly applies to the L-mode and ITB plasmas we have analysed) because of the different pressure scale lengths for the main and impurity ion species. We conclude that the simplified approach of Ref.[15] may not be completely adequate to capture the essential features of the neoclassical calculation of V_θ. On the other hand, Fig.1 convincingly shows that the intuitively simpler (computationally much faster) analytical formulation developed here indeed reproduces sufficiently well the complete NCLASS calculations.

Since it has not yet been convincingly demonstrated that indeed $V_{\theta C}(x,t)$ is neoclassical, the use of such value for computing $E_r(x,t)$ is obviously introducing an error which is difficult to quantify, particularly at the plasma edge where we can clearly have that $|V_\theta/V_\phi|\approx O(|B_\theta/B_\phi|)$ due to the low

toroidal momentum input. Hence, all the results presented in the following sections have to be taken with the caveat of having used the neoclassical value for $V_\theta(x,t)$, therefore the calculated radial electric field $E_r(x,t)$ is obviously to be intended purely as the neoclassical one.

6. ERROR ANALYSIS.

An accurate and systematic error analysis is needed in order to assess the validity and the possible applications of the various models proposing the spatial and temporal evolution of the radial electric field as a crucial parameter for the transition to high confinement regimes. Here we estimate the total uncertainty on the neoclassical calculation of $E_r(x,t)$ using a Gaussian propagation of the errors on the measured quantities which enter the formulation presented in Section 4. Note that for our error analysis we assume that the spatial grid $x=\sqrt{\psi_N}$ where the measurements are made is known exactly a-priori, i.e., to be free from errors. Typical values for the statistical absolute error σ on the magnetic field and safety factor profiles are $\sigma(B_\phi)\approx0.05B_\phi$ (due to uncertainties in the current in the main toroidal field solenoid) and $\sigma(q)\approx0.1q$, giving for the poloidal field $\sigma(B_\theta)\approx0.12B_\theta$; on the electron density profile $\sigma(n_e)\approx0.1n_e$ in the plasma core and $\sigma(n_e)\approx0.3n_e$ at the plasma edge, for $x>0.85$; on the carbon density and toroidal rotation velocity, ion temperature and effective charge profiles $\sigma(n_C)\approx0.3n_C$, $\sigma(V_{\phi C})\approx0.15V_{\phi C}$, $\sigma(T_i)\approx0.05T_i$, and $\sigma(Z_{EFF})\approx0.2Z_{EFF}$, respectively. The error on the deuterium density profile $n_D(x)$ depends on $\sigma(Z_{EFF})$, $\sigma(n_e)$ and $\sigma(n_C)$ through conservation of the local charge neutrality (see also Section 7) $\Sigma_i Z_i n_i(x)=n_e(x)$ and of $Z_{EFF}(x)=\Sigma_i n_i(x)Z_i^2/n_e(x)$, if used, given $n_C(x)$, $Z_{EFF}(x)$ and $n_e(x)$: hence we typically have that $\sigma(n_D)\approx0.4n_D$.

In addition to the statistical error, a recent calibration of the CX diagnostic has provided for the first time the evaluation of the systematic error on n_C, hence n_D, which are related to the calculation of the active CX volume [10]. These systematic errors, of the order of $\sigma_{SYST}\sim10\%$ are important to evaluate the uncertainty on the calculated E_r for a single pulse, but obviously can be neglected when comparing various discharges for which the same absolute calibration applies. The systematic errors on the CX measurements are shown in Fig.2 for one of the calibration shots, where the labels in the legend indicate different methods for computing the CX active volume.

To the Gaussian propagation of the uncertainty on the basic plasma measurements, we have added a "most probable" estimate of the error due to taking the gradients of these data, as in the calculation of the scale lengths. Consider now a quantity $y(x)$ described by a Gaussian probability distribution function $P[y_{(x=x1)}=y_1]=\exp[-(y-y_1)^2/\sigma^2(y_1)]$, where $\sigma(y_n)$ is the uncertainty on the measured $y(x=x_n)$: hence we have that, for instance, $P[y_{(x=x1)}=y_1\pm\sigma(y_1)]=(1/e)\times P[y_{(x=x1)}=y_1]$. Therefore the error on the gradient (dy/dx) between the two points x_2 and x_1 can be defined as:

$$\int_{y1-z\sigma}^{y1+z\sigma} dy\, P(y) = \int_{y1-z\sigma}^{y1+z\sigma} dy\, exp\left[-\frac{(y-y_1)^2}{\sigma^2(y_1)}\right] = 1,\ \sigma\left(\frac{dy}{dx}\right)_{x1\leftrightarrow x2} = \sqrt{\pi}\ \sqrt{erf(z)}\ \sqrt{\sigma(y_1)\ \sigma(y_2)}.\quad (12)$$

Here z is given by $P[y_{(x=x1)}=y_1\pm(z+\varepsilon)\sigma(y_1)]=0$ for $\varepsilon=o(z)$. Since erf(z)≈1 with d[erf(z)]/dz≈0 for z≥3, we can now consider the practical cases z=1→3: hence the error on taking the gradient between two points is approximately $\sqrt{\pi}*\sqrt{erf(1\rightarrow3)}\approx1.63\rightarrow1.77$ larger than the usual geometric error, and overall can account for up to approximately 25% of the total error on E_r. This probabilistic approach to evaluate the error on the gradient is conceptually different from the result obtained by taking the Gaussian propagation of the errors on the two y-points, $\sigma_{GAUSS}(dy/dx)=[\sigma^2(y_1)+\sigma(y)]^{1/2}$. As an example, consider the case $\sigma(y_2)\approx\sigma(y_n)$: we have that $\sigma(dy/dx)/\sigma_{GAUSS}(dy/dx)\approx\sqrt{\pi}\sqrt{erf(3)}/\sqrt{2}\approx1.25$. Hence the error on the gradient, as defined in probabilistic terms by Eq.(12), is generally larger than that given by the Gaussian propagation of the errors on the two data points $[y_1,y_2]$. Only in the case of locally poor raw measurements such that $\sigma(y_1)>>\sigma(y_2)$ we have that the probabilistic error is less then the Gaussian one, $\sigma(dy/dx)/\sigma_{GAUSS}(dy/dx)\approx1.77[\sigma(y_2)/\sigma(y_1)]^{1/2}<1$, but obviously this situation is not one that should be considered as ideal for further detailed theoretical and modelling analysis. The advantage of using Eq.(12) to determine the error on the gradient, instead of the more common Gaussian propagation, is that we can give the correct weight to the probability of a certain gradient to occur between two points, which allows us to avoid unphysical results in our error analysis.

Simplified analytical expression for the statistical error on the computed deuterium toroidal rotation velocity, carbon and deuterium poloidal rotation velocity and radial electric field are thus given by:

$$\sigma(V_{\phi D})=\sqrt{\sigma^2(V_{\phi C})+(V_{\phi D}-V_{\phi C})^2\left[\bar{\sigma}^2(K_2)+\bar{\sigma}^2(B_\theta)+(1-F_1)^2\bar{\sigma}^2(\nabla T)\right]},\qquad(13a)$$

$$\bar{\sigma}(V_{\theta D})=\sqrt{\bar{\sigma}^2(K_1)+\bar{\sigma}^2(B)+(1-F_1)^2\bar{\sigma}^2(\nabla T)},\qquad(13b)$$

$$\sigma(V_{\theta C})=\sqrt{\bar{\sigma}^2(K_1)V_{\theta C}^2+XV_{\theta D}^2+F_0^2\sigma^2(V_{\theta D})},\qquad(13c)$$

$$\sigma(E_{rD})=\left\{\left(\frac{\nabla p_D}{eZ_Dn_D}\right)^2\bar{\sigma}^2(n_D)+\left[(1-F_2)\frac{T_i}{L_{pD}eZ_D}\right]^2\bar{\sigma}^2(\nabla p_D)+\right.$$
$$\left.+B_\phi^2\left[\sigma^2(V_{\theta D})+V_{\theta D}^2\bar{\sigma}^2(B_\phi)\right]+B_\theta^2\left[\sigma^2(V_{\phi D})+V_{\phi D}^2\bar{\sigma}^2(B_\theta)\right]\right\}^{1/2},\qquad(13d)$$

$$\sigma(E_{rC})=\left\{\left(\frac{\nabla p_C}{eZ_Cn_C}\right)^2\bar{\sigma}^2(n_C)+\left[(1-F_3)\frac{T_i}{L_{pC}eZ_C}\right]^2\bar{\sigma}^2(\nabla p_C)+\right.$$
$$\left.+B_\phi^2\left[\sigma^2(V_{\theta C})+V_{\theta C}^2\bar{\sigma}^2(B_\phi)\right]+B_\theta^2\left[\sigma^2(V_{\phi C})+V_{\phi C}^2\bar{\sigma}^2(B_\theta)\right]\right\}^{1/2}.\qquad(13e)$$

In Eqs.13(a)-13(e) $\bar{\sigma}(X)=\sigma(X)/X$ indicates the relative statistical error on the quantity X and:

$$\bar{\sigma}(K_1)\approx\bar{\sigma}(K_2)=\frac{Z_Cn_C}{Z_Dn_D}\sqrt{\bar{\sigma}^2(n_C)+\bar{\sigma}^2(n_D)},\qquad(14a)$$

$$X = \sigma^2(K_1) + 2.25\sigma^2(K_2) + \frac{L_{TD}^2}{L_{pD}^2}\left[F_1^2 L_0^2 \overline{\sigma}^2(\nabla T) + F_2^2 \overline{\sigma}^2(\nabla p_D) + \frac{Z_D^2 L_{pD}^2}{Z_C^2 L_{pC}^2} F_3^2 \overline{\sigma}^2(\nabla p_C)\right], \quad (14b)$$

$$L_0 = 1 - \frac{Z_D L_{pD}}{Z_C L_{pC}}, \quad F_0 = K_1 + 1.5 K_2 - L_0 \frac{L_{TD}}{L_{pD}}, \quad (14c)$$

$$F_1 = sign(L_{TD})\frac{\partial \log|L_{TD}|}{\partial \log T}, \quad F_2 = sign(L_{pD})\frac{\partial \log|L_{pD}|}{\partial \log p_D}, \quad F_3 = sign(L_{pC})\frac{\partial \log|L_{pC}|}{\partial \log p_C}. \quad (14d)$$

The systematic error on the computed $V_{\phi D}$, $V_{\theta C}$ and $V_{\theta D}$, E_{rC} and E_{rD} is obtained by substituting $\sigma_{SYST}(n_C) \rightarrow \sigma(n_C)$, $\sigma_{SYST}(n_D) \rightarrow \sigma(n_D)$ and $\sigma_{SYST}(T) \rightarrow \sigma(T)$ in Eqs.(13,14), with $\sigma_{TOT} = (\sigma^2 + \sigma^2_{SYST})^{1/2}$.

7. E-FIELD//NCLASS COMPARISON FOR A REFERENCE L-TO-H MODE PLASMA.

The steady-state L- and H-mode phases of Pulse No: 57819 have been chosen here for a detailed comparison between the JETTO and NCLASS codes and our analytical formulation (referred to with the label "E-field" in the following), and for a systematic assessment of the difference in $E_r(x,t)$ resulting from the various constraints on the processing of the raw input data. Note that JETTO and NCLASS use by default the same input data, which can also be used by E-field for a direct comparison allowing the separation between the role of input profiles and that of the analytical approximation employed by E-field. Figure 3 shows the main plasma and magnetic field data for this discharge: note $T_i \approx T_e$. The various profile quantities were computed using spline fit interpolation, and n_D was obtained using the measured n_C and n_e and conservation of local charge neutrality, $n_e = n_C Z_C + n_D Z_D$.

A possible source of uncertainty in determining $E_r(x,t)$ comes from the fact that the input data for the neoclassical calculation are measured on different spatial and temporal grids, and thus need to be inter- and extrapolated onto the same (x,t)-grids. This is done in E-field using either linear, spline or cubic (with Hermite polynomials) fitting routines, with the constraint that the fitted values are within the s-confidence level of the measurement. The fitting routines implemented in JETTO and NCLASS do not use a similar constraint, hence these often produce different input data profiles. The differences resulting from the application of these methods are demonstrated in Fig.4, which shows various input plasma data and computed neoclassical quantities for the H-mode phase of Pulse No: 57819, for which the CX measurements were available in the region 3.15<R(m)<3.8. As expected, there is no difference between the cubic, spline and linear fitting methods when interpolating over the range of the CX measurements. Conversely, we notice the clear differences between these three methods when extrapolating the CX data towards the magnetic axis (R=2.93m) and the plasma boundary (the last closed flux surface from the equilibrium reconstruction is located at R=3.98m), with clear implication on the computed $V_{\phi D}$, $V_{\theta C}$ and $V_{\theta D}$, hence $E_r(x,t)$. The choice of the fitting method can in principle affect the resulting E_r at the plasma edge and in the plasma core due to the complex dependency of $E_r(x,t)$ on the temperature, density and pressure gradients. Hence, for the E_r calculations presented in Sections 8 and 9, we have first considered all the three fitting methods indicated above, then chosen a reference one, and have only accepted the result if

the difference in E_r when using the other two methods is below the estimated total error:

$$\sigma_{TOT}(E_r) = \left\{ \sigma^2(E_{r1}) + 4\left(\frac{E_{r2} - E_{r1}}{E_{r2} + E_{r1}}\right)^2 \sigma^2(E_{r2}) + 4\left(\frac{E_{r3} - E_{r1}}{E_{r3} + E_{r1}}\right)^2 \sigma^2(E_{r3}) \right\}^{1/2} . \qquad (15)$$

Here E_{rX} and $\sigma(E_{rX})$ are the values of E_r and $\sigma(E_r)$ evaluated using the reference choice of numerical method (subscript 1), and the other two alternative choices (subscripts 2 and 3), respectively.

Two additional constraints for fitting and inter/extrapolating the ion density profiles may be given by conserving the local charge neutrality, $\sum_i n_i Z_i = n_e$, and the effective charge $Z_{EFF} = \sum_i n_i Z_i^2 / n_e$, which can be directly measured via Bremsstrahlung or constructed using a-priori knowledge of all the ion and impurity density profiles. It must be noted here that in the framework of the neoclassical theory of Ref.[7], only carbon and deuterium should be considered in determining Z_{EFF}, whereas the Bremsstrahlung measurements include the contribution of all impurity species, mainly B_e, H_e and H for the JET plasmas considered here. As an illustration of the differences that may arise when using additional impurities to evaluate the ion density profiles, we have compared two approaches. First, we use the measured n_e and n_C and local charge neutrality $n_C Z_C + n_D Z_D = n_e$ to deduce the n_D profile. Second, we consider the Z_{EFF} profile from Bremsstrahlung, then include only B_e, H_e and H keeping a fixed ratio for B_e/C, H_e/C and H/D as given by the spectroscopic and D_a/H_a measurements in the divertor and at the plasma edge (measurement of the radial profiles of these ratios are not available), and compute the n_C, n_D and n_e profiles to conserve the local charge neutrality. With this approach, we have now obtained an $n_e(x,t)$ consistent with Z_{EFF} from Bremsstrahlung which, however, does not necessarily match the measured $n_e(x,t)$ (using LIDAR and interferometer). With this approach, n_D is typically ~20% lower in magnitude, with no significant change in the shape of the profile, whereas the n_C profile can vary by more than ~50%, particularly just inside the edge pedestal region due to the presence of B_e (and H_e to a minor extent). Figures 5(a) and 5(b) show a comparison of the deuterium and carbon density profiles obtained using these two methods for the L- and H-mode phase of Pulse No: 57819, which clearly illustrate the differences in the resulting n_C and n_D profiles. In the following, due to the rather arbitrary choice of keeping a fixed ratio for the B_e/C, H_e/C and H/D profiles because of lack of spatially resolved measurements, we have used the measured n_e and n_C (from the absolutely calibrated CX measurements) and we have imposed the local charge neutrality $n_e = n_C Z_C + n_D Z_D$ as a constraint to deduce the $n_D(x,t)$ profile. The JETTO code computes the ion density profiles using local charge neutrality and an input Z_{EFF}, taken from the Bremsstrahlung data or a user-choice profile. This significantly affects the calculation of the density and pressure gradients, particularly at the plasma edge, producing a further difference in the output $E_r(x,t)$.

A further point to consider here is the radial averaging of the input data, and particularly the role of the ion orbit width. The JETTO and NCLASS codes do not consider averaging over the ion banana or potato orbit width, $\delta_{BAN} \approx q\rho_\theta/\sqrt{\varepsilon}$ and $\delta_{POT} \approx R_0(4q\rho_\phi/R_0)^{2/3} \approx 20(\varepsilon/q)\delta_{BAN}$, respectively, whose main effects are to slightly shift inwards and largely smooth out the radial gradients in the temperature, density and pressure profiles. An example of this smoothing over the banana, potato and effective ion orbit width δ_{ORB}, as per Eq.11(c), is given in Figs.6(a) and 6(b) for the calculated

13

poloidal rotation velocity and toroidal rotation frequency during the L- and H-mode phase of Pulse No: 57819, respectively. As the reference case without orbit-averaging, we have considered the results obtained using spline fitting without Z_{EFF}-normalisation of the ion density profiles. During the L-mode phase, we notice the clear smoothing of the double-hump structure in $V_{\theta C}$ and $V_{\theta D}$ in the plasma core, for $0.2<x<0.4$. During the H-mode phase, note the disappearance of the large and broad peak in $V_{\theta D}$ around mid-radius, and of the somewhat narrower peak in $V_{\theta C}$ towards the plasma boundary. Note also that the orbit-width average value can be globally lower than the non-averaged one since we have used a "rolling" averaging process. The orbit-width averaged value computed at an inner radius is used to infer the orbit-width averaged value at the outer radius, starting from the magnetic axis towards the plasma boundary and then reversing the direction of the averaging process to remove artificial (i.e., purely numerical) radial shifts in the overall profile.

Figure 7(a) shows the effect of the different numerical schemes used by E-field to calculate E_r for Pulse No: 57819 at t=3.5sec, during the L-mode phase. First, we note the excellent agreement between E_{rC} and E_{rD}, which proves in principle the validity of the analytic approximations developed and used here. The choice of the numerical routines for inter/extrapolating is only important in the plasma core, where the difference between the various E_r's is beyond the typical error bar. For the case of spline fitting, the effect of the Z_{EFF}-normalisation from Bremsstrahlung is negligible because of cancellation between the poloidal and pressure gradient component of E_r. On the other hand, orbit-width averaging slightly modify $\nabla p/n$, hence E_r, in the plasma core, in the region $\delta_{BAN}<\rho<2*\delta_{POT}$, where $\delta_{BAN}\sim$3cm and $\delta_{POT}\sim$15cm. Similarly, Fig.7(b) shows the effect of the numerical schemes used by E-field to calculate E_r for Pulse No: 57819 at t=7.85sec, during the steady-state H-mode phase. Here the effect of the different numerical routines used for inter/extrapolating is less apparent, since the "raw" data profiles are smoother, whereas that of Z_{EFF}-normalisation of the ion density profile (using the Bremsstrahlung data) is much more evident, increasing E_r by about 40% towards mid-radius. We notice also the different sign of E_r at the top of the pedestal, for $0.8<x<0.9$, which is due to a non-exact cancellation between the poloidal and pressure gradient component of E_r. This can have important implications for associating the L-H transition to changes in E_r at the plasma edge.

In summary, we conclude that the use of spline fitting routines for the input radial profiles may sometimes lead to unphysical results when extrapolating if the second derivative of the raw data goes through a zero and/or changes sign just before the region where extrapolation is needed. This is a well-known problem, and care must be taken when using such spline-fitting routines. We find that averaging over the ion orbit width smoothes out radial gradients, a numerically and physically sound result. We have also clearly demonstrated the (obvious, but too often underestimated) role of the Z_{EFF}-normalisation when computing the ion density profiles. This may lead to rather significant changes in E_r due to its pressure gradient component, particularly towards the edge pedestal region where the usually dominant toroidal component of E_r becomes small. The solution to this problem is not clear: the neoclassical theory presented in Ref.[7], and its implementation in most transport codes such as JETTO [11] and NCLASS [12], considers only one main ion and one impurity ion

species, therefore Z_{EFF} from Bremsstrahlung cannot be used in the calculation, but on the other hand the typical JET plasmas contain a few more ion species than simply carbon and deuterium. Hence, we have empirically dealt with this difficulty by adding a further term to the error bar on the ion density profiles and Z_{EFF}, which contributes to about 10% of the total error on $E_r(x,t)$:

$$\sigma(n_D) = \frac{1}{2Z_D}\sqrt{\sigma^2\left(n_e\left(1+\frac{Z_{EFF}^2}{Z_D^2}\right)\right) + Z_C^2\sigma^2\left(n_C\left(1+\frac{Z_C^2}{Z_D^2}\right)\right) + \frac{n_e^2}{Z_D^2}\sigma^2\left(Z_{EFF}\right)}, \qquad (16a)$$

$$\sigma\left(Z_{EFF}\right) \approx \sigma(Z_{EFF})\sqrt{1+\frac{Z_{EFF}^{(BREM)}-Z_{EFF}}{n_C Z_C^2 + n_D Z_D^2}} \ . \qquad (16b)$$

To conclude this section, Figs.8(a) and 8(b) show the comparison of the flux-surface averaged E_{rC} and E_{rD} calculated with NCLASS and E-field at t=4.0sec, during the L-mode phase; Figs.9(a) and 9(b) show E_{rC} and E_{rD} at t=8.1sec, during the steady-state H-mode phase. In Figs.8 and 9 (and in the following) the label "E-JETTO" indicates that the E-field code was run using the JETTO input profiles (also used by NCLASS). Hence comparing "E-field" with "E-JETTO" allow us to assess the role of a different numerical treatment of the input data, whereas comparing""E-JETTO" with "NCLASS" elucidates the role of the analytical approximations used here. We used linear fitting for this E-field calculation, with n_D computed from the measured n_C and n_e profiles using local charge neutrality, without orbit width averaging (as in NCLASS). Note that the JETTO/NCLASS standard output is the ion-mass-density averaged, flux-surface averaged radial electric field:

$$E_{r,CD} = \left\langle \frac{n_C A_C E_{rC} + n_D A_D E_{rD}}{n_C A_C + n_D A_D} \right\rangle. \qquad (17)$$

As demonstrated in Fig.8(b) and Fig.9(b), using E-field we obtain $E_{rC}(x,t)=E_{rD}(x,t)$ within the error bar in the calculation, thus mass averaging does not affect the value of E_r: $E_{r,CD}(x,t)=E_{rC}(x,t)=E_{rD}(x,t)$.

First, we notice that during the steady-state L-mode phase (Figs.8(a), 8(b)), where the ion density and temperature profiles are rather flat up to x<0.8, the differences between E-field and E-JETTO are mainly due to the different fitting of the measured $V_{\phi C}$. The NCLASS and E-JETTO values of $E_r(x,t)$ are in very good agreement in the region 0.1<x<0.9, which also indicates the validity of the analytic treatment of the toroidal flux-surfaces. Conversely, we notice that $\nabla p \neq 0$ with NCLASS on the magnetic axis, hence E_r becomes (incorrectly) large and negative in the plasma core, and it does not agree with the E-field and E-JETTO values. The discrepancy in E_r at the plasma edge (x>0.9) is essentially due to the different Z_{EFF}, hence the ion density profiles, which in turn affects $\nabla p/n$.

Second, we notice that during the steady-state H-mode phase (Figs.9(a), 9(b)) the numerical fitting methods in JETTO/NCLASS do not reproduce well the typical H-mode edge pedestal in the density and toroidal rotation, around x≈0.9. This, together with the different Z_{EFF}-normalisation of the ion density profiles (JETTO/NCLASS use the Bremsstrahlung value), affects the edge value of $E_r(x,t)$: $E_r<0$ for 0.85<x<0.95 with E-field due to the pressure gradient component of E_r, but $E_r≈10$kV/m with NCLASS. As for the L-mode phase, $E_r<0$ (incorrectly) on the magnetic axis with NCLASS, but overall there is an excellent agreement between the E-field and JETTO/NCLASS calculations.

8. CALCULATION OF E_r FOR

A) L-MODE PLASMAS.

Having checked in Section 7 the general use of the E-field code in comparison with JETTO and NCLASS, we now turn our attention to the analysis of E_r for L-mode plasmas so as to build some understanding of the possible role of E_r in the L-H transition, which will be discussed throughout Section 8B. As an example of a JET L-mode pulse, we consider here Pulse No: 58263, for which the main plasma parameters are shown in Fig.10: we note that diagnostic P_{NBI}=1.6MW was used to supplement the main Ion Cyclotron Resonance Frequency (ICRF), P_{RF}=4MW. Figures 11(a) and 11(b) show the input data and the E_r profiles calculated at t=20.0sec during the steady-state phase of the discharge, indicating the broadly general agreement between the E-field and NCLASS results but for $V_{\theta D}$. Here the E_r calculation was performed using spline fitting, with $n_D(x)$ computed from the measured $n_C(x)$ and $n_e(x)$ using local charge neutrality, with no orbit width averaging for a closer comparison with the NCLASS results. We note in this respect that for the case of low-temperature ($<T_i>\approx<T_e>\approx$3keV) L-mode plasmas with a monotonic q-profile, orbit width averaging does not introduce a significant difference in the E_r calculation because the density and temperature profiles are rather flat and we have as well that $\delta_{BAN}\approx$3-8cm, $\delta_{POT}\approx$10cm, with $F_{POT}/F_{BAN}<$0.01.

First, there is a small difference in the toroidal component of E_r around mid-radius, which is due to the different numerical treatment of the input $V_{\phi C}$ profile. Second, and more importantly, we notice immediately that the toroidal component of E_r goes to zero for x>0.85 since $V_{\phi C}\approx V_{\phi D}\rightarrow$0 because of a negligible momentum input. This implies that the balance between the pressure and poloidal component becomes the dominant contribution to E_r at the plasma edge. Hence different approaches to compute the n_C and n_D profiles (conserving charge neutrality with/out Z_{EFF}-normalisation using the Bremsstrahlung data) will lead to significant differences for the calculated E_r at the plasma edge, as clearly shown in Fig.11(b): $<E_{r,CD}>\approx$-10kV/m with NCLASS but $E_r\approx$0 with E-field and E-JETTO, because of a difference balance between the $V_\theta\times B_\phi$ and $\nabla p/n$ components at the plasma edge. With the above-mentioned caveat for the edge region x>0.9, from the analysis of various JET L-mode pulses we generally infer that E_r has a rather flat radial profile in the region 0.2<x<0.85, with $E_r\approx$5÷15kV/m (depending on P_{NBI}, hence the toroidal rotation profile), very rapidly dropping to (possibly) negative values via a steep density gradient at the far edge of the plasma, $-5<E_r$(kV/m)<0 for x>0.95, where the balance between its poloidal and pressure components dominates E_r.

B) THE L-H MODE TRANSITION.

Having established in Section 8A the main features of E_r during steady-state L-mode plasmas, we now turn our attention to the radial and temporal evolution of E_r(x,t) during the L-H transition. To this aim, we consider here JET Pulse No: 57819, where the L-H transition occurs around t=4.3sec when P_{NBI} increases from P_{NBI}=4MW to P_{NBI}=8.6MW (Fig.3 shows the main plasma parameters for this pulse). Figures 12(a) and 12(b) show the profile E_{rC}(x,t) ($\approx E_{rD}$(x,t)), normalised with respect to the total $P_{NBI}+P_{RF}$ power deposition profile r_{DEP}, for Pulse No: 57819 and the reference L-mode

Pulse No: 58263 discussed in section 8A, respectively. Here spline fitting was used, with $n_D(x)$ computed from the measured $n_C(x)$ and $n_e(x)$ maintain local charge neutrality, and E_{rC} was then averaged over the effective ion orbit width, $\delta_{ORB} \approx 8cm$ for Pulse No: 58263 and $\delta_{ORB} \approx 12cm$ for Pulse No: 57819, respectively. The normalisation of E_r with respect to ρ_{DEP} is important in order to take into account possible variations in the shape of E_r which would be solely due to a different momentum input, i.e. not related to an improving (or deteriorating) plasma confinement. Furthermore, the edge values of the ion density and Z_{EFF} not only affect the magnitude of $E_r(x,t)$ and its shape, but similarly affect $\rho_{DEP}(x,t)$, hence the ratio E_r/ρ_{DEP} becomes less sensitive to the details of $Z_{EFF}(x,t)$ and $n(x,t)$ than $E_r(x,t)$ alone. Here we have computed $\rho_{DEP}(x,t)=\rho_{NBI}(x,t)+\rho_{RF}(x,t)$ using a beam deposition code [21] for the NBI component and hot-plasma wave dispersion [22] for the ICRF component, respectively.

For Pulse No: 57819, we notice the clear increase in E_{rC} at the L-to-H transition (indicated by the black horizontal line) in the region $0.4<x<0.7$ over ~200ms, with a subsequent very sudden transient drop over ~100ms, followed by a steady increase (with no profile broadening) as V_ϕ and $\nabla p/n$ build up in the region $0.25<x<0.75$. Conversely, there is no significant difference around the edge pedestal at the L-H transition, but this result relies heavily on the method used to compute the ion density profiles. For Pulse No: 58263, we notice the broadly flat E_r/ρ_{DEP} profile over the region $0.2<x<0.8$; again, the fine structure details appearing for $x>0.9$ depend heavily on the n_C and Z_{EFF} profiles used here. Similarly, we point out that the result $E_r<0$ for $x>0.75$ is a clear feature of NBI-dominated plasmas.

C) H MODE PLASMAS WITH NORMAL AND REVERSED ION ∇B-DRIFT DIRECTION.

The ion ∇B-drift direction is an important parameter in determining the accessibility conditions for the H-mode regime. There is clear experimental evidence that the H-mode regime is obtained at a lower input power level (typically a factor two) when the ion ∇B-drift is directed towards the divertor than when it is in the opposite direction, i.e. in situations when only the magnetic field is reversed, but not the plasma current [23]. However, recent JET data have provided evidence that the H-mode power threshold is similar for the two ion ∇B-drift directions across a range of magnetic field $B(T)=1.2-3.0$ and low edge electron density, $n_e(edge)<2x10^{19}m^{-3}$ [24]. These results have been obtained when reversing both the current and the magnetic field, conserving the plasma helicity. Hence, the similar power threshold may be related to the different momentum input at the plasma edge from the beam ions, including possible prompt losses, with clear implications on the edge values of $V_\phi(x,t)$ and $\nabla p(x,t)$, hence $E_r(x,t)$. It is thus important to assess the difference in $E_r(x,t)$ at the L-H transition and during steady-state H-mode phases as function of the ion ∇B-drift direction. Figure 13 shows the main plasma parameters for Pulse No: 59624, a typical L-to-H mode pulse with reversed current and toroidal magnetic field, giving rise to an ion ∇B-drift directed away from the strike points and the divertor target plates. We note that in JET B_ϕ and I_p are reversed together, i.e. the plasma helicity does not change between the reversed (RBE) and forward (FBE, which is the normal case for JET) B-field case. Figures 14(a) and 14(b) show some of the neoclassical

collisionality factors entering the calculation of $V_{\phi D}$, $V_{\theta C}$ and $V_{\theta D}$ for Pulse No: 59624 and Pulse No: 57819, to elucidate possible differences due the ion ∇B-drift direction. Despite the factor ~2 difference in $\nu_{*i} \propto \varepsilon^{-3/2}$ in the plasma core and in $\nu_{*i} \propto (B/\nabla B)^2$ at the plasma edge, we note that $K_1(x,t)$ and $K_2(x,t)$ are very similar and sufficiently independent of the ion ∇B-drift direction, thus indicating that in both configurations the main and impurity ion species are effectively in the banana regime.

Figure 15 shows the 3D profile $E_{rC}(x,t)$ ($\approx E_{rD}(x,t)$) calculated with the E-field code: this calculation was performed using spline fitting, with $n_D(x)$ computed from the measured $n_C(x)$ and $n_e(x)$ using local charge neutrality, with E_r normalised with respect to the total $P_{NBI}+P_{RF}$ power deposition profile, and averaged over the ion orbit width. Following the conventional JET sign convention for the magnetic topology, a negative E_r is now pointing outwards towards large major radii, as it is the case with forward-B for a positive E_r. We notice that the change in the ELM behaviour at t=4.5sec, from Type-I to Type-III, only significantly affects the magnitude of $E_r(x,t)$ in the region 0.6<x<0.9 due to a change in the scale lengths, reducing its peaking but only marginally modifying its overall shape. In comparison with Fig.12(a), we note immediately the different shape of $E_r(x,t)$ with the reversed ion ∇B-drift direction, particularly in the region 0.6<x<0.9. With the reversed ion ∇B-drift direction $E_r(x,t)$ has a broadly flat profile over the region 0.3<x<0.7, contrary to the normal ion ∇B-drift direction, where $E_r(x,t)$ has a hollow radial profile towards the plasma edge, that can be approximated with a quasi-Gaussian shape $E_r(x) \propto \exp(-(x-x_0)^2/W_{ER}^2)$ peaked around $x_0 \approx 0.6$ with half-width at half-maximum of the order of $W_{ER} \approx 0.15$.

To assess in further details the possible role of the prompt NBI losses at the plasma edge in the reverse ion ∇B-drift direction, we have considered two further RBE pulses at higher B_ϕ and I_p, Pulse No:59647 with B_ϕ/I_p=2.4T/2MA and Pulse No: 59644 with B_ϕ/I_p=3T/3MA, respectively, in comparison with the reference H-mode FBE Pulse No: 57819 with B_ϕ/I_p=1.7T/1.4MA, and the reference L-mode FBE Pulse No:58263 with B_ϕ/I_p=2.7T/2.5MA. The higher I_p in the last two RBE pulses improves the confinement of the NBI ions at the plasma edge, hence empirically affecting the NBI-driven density, temperature and rotation profiles. Note that the high B_ϕ/I_p RBE pulse (Pulse No: 59644) shows a dithering L-to-H mode transition. Figure 16(a) shows the main plasma parameters and collisionality data for the RBE pulses during the (steady-state for Pulse No: 59624 and Pulse No: 59647) H-mode phase, and Fig.16(b) shows the calculated orbit-width (flux-surface averaged) radial electric field for the three RBE and the two reference FBE pulses. Here E_r was computed using spline fitting, with $n_D(x)$ obtained from the measured $n_C(x)$ and $n_e(x)$ using local charge neutrality. The result was normalised with respect to the input $P_{NBI}+P_{RF}$ power deposition profile $\rho_{DEP}(x)$ (Pulse No: 59624, t=9.0sec: P_{NBI}=12.0MW; Pulse No: 59647, t=3.5sec: P_{NBI}=12.1MW; Pulse No: 59644, t=8.5sec: P_{NBI}=13.7MW; Pulse No: 57819, t=8.0s: P_{NBI}=8.7MW, and t=4.0sec: P_{NBI}=4.0MW, the H-mode and dithering L-H mode reference FBE cases, respectively; Pulse No: 58263, t=20.0sec: P_{NBI}=1.7MW, PRF=4.0MW, the L-mode reference FBE case). We notice the clear differences in the E_r/ρ_{DEP} profile between the RBE and the FBE cases, both in shape and magnitude, beyond those that can be accounted for by the variation in the input $\rho_{DEP}(x)$.

The FBE discharge at higher plasma current (Pulse No:59644) has the E_r/ρ_{DEP} more closely resembling that of the reference FBE pulses (which moreover had both a lower I_p and P_{NBI}). In particular, we note that at low field/current E_r/ρ_{DEP} is very flat across the poloidal cross-section, and that it is negligible at the plasma edge. Conversely, at higher B_ϕ/I_p the RBE pulse shows a marked gradient in E_r/ρ_{DEP} at the plasma edge, around $x \approx 0.9$, similarly to the reference H-mode and L-mode FBE cases, although in the latter case the gradient is not so sharp. We also wish to point out that indeed for this particular comparison, as indicated in Fig.16(b), the edge values of the ion density and Z_{EFF} affect the magnitude of $E_r(x,t)$, but not its overall shape, and moreover the same density profiles similarly affect $\rho_{DEP}(x,t)$. Hence the ratio E_r/ρ_{DEP} becomes less sensitive to the $Z_{EFF}(x,t)$ and $n(x,t)$ used in the calculation than $E_r(x,t)$ alone.

In summary, the observations reported here empirically confirm the role of the prompt NBI losses at the plasma edge in determining the radial electric field profile. This can have important implications for the L-H transition studies as function of the direction of the ion ∇B-drift, and clearly points to the need of matching also the plasma helicity when performing multi-machine comparison studies of the L-H transition. Hence the JET and Asdex-U results [24, 23] that have been recently reported warrant a further detailed comparison in light of the different plasma helicity in these studies.

9 CALCULATION OF E_r FOR

A) ITB PLASMAS.

In Sections 8A to 8C we have analysed the role of $E_r(x,t)$ during the transition to high-confinement regimes in the conventional tokamak scenario, with a monotonic q-profile, hence positive magnetic shear $s=(r/q)(dq/dr)$, typically with $q_0<1$. These regimes are characterised by a flat pressure profile across the core region of the plasma, which is supplemented by a large edge pedestal (hence with strong pressure gradients) when in H-mode. In this section we focus on the advanced tokamak scenarios that are used in JET, which are characterised on the other hand by a non-monotonic (or at least very flat) q-profile with $q_0 \approx 2$, hence a negative magnetic shear in the plasma core. In these configurations a strong pressure gradient, hence an internal transport barrier (ITB), develops around mid-radius, which is sometimes supplemented by an additional transport barrier at the plasma edge when in H-mode [2]. These configurations are precisely those where the neoclassical theory is potentially expected to break-down, since $\rho_{\theta C,D} \approx L$'s in the plasma core due to the much lower local current density. As an example of this condition, for a typical steady-state plasma with the ITB located around $x=0.35$, we have that the orbit-width averaged $\langle\rho_{\theta D}/L_{pD}\rangle \approx 2$ in the region $x<0.2$, and only well outside the ITB foot we have that $\langle\rho_{\theta D}/L_{pD}\rangle \approx 0.5$. The region inside the ITB location is, strictly speaking, beyond the limits of applicability of the neoclassical theory used to derive $V_{\phi D}$ and V_θ, hence $E_r(x,t)$. For consistency with the approximations used in the neoclassical theory of Ref.[7], in the following sub-sections on ITB plasmas we have therefore restricted our analysis only to those regions where $\rho_{\theta D}(x,t)/L_{pD}(x,t)=O(\varepsilon)$.

B) ITB PLASMAS: HIGH PERFORMANCE ITB WITH LARGE POTATO ORBITS.

As an example of a high performance ITB with large ion temperature gradient ∇T_i we consider now Pulse No: 61349, for which Fig.17 shows the main plasma parameters and Fig.18(a) and Fig.18(b) show the input data for the neoclassical calculation of $E_r(x,t)$ at t=6.1sec, at the peak time in $T_i(x,t)$, and at x=0.38 (R=3.35m), the ITB position, corresponding to that of the peak $T_i(x,t)$. Here $T_i(x=0)\approx20$keV and ∇T_i reaches the value of ~250keV/m around x=0.4, across the position of the ITB. The data shown in Fig.18 have been computed using spline fitting, with $n_D(x)$ computed from the measured $n_C(x)$ and $n_e(x)$ using local charge neutrality, and averaging over the effective ion orbit width $\delta_{ORB}(x)$. It should be noted here that $\rho_{\theta D}(x,t)=O(L_{pD}(x,t))$ for x<0.2, hence the neoclassical theory is not strictly applicable in the plasma core. Notice the good agreement in the shape of the calculated $V_\theta(x,t)$, the difference in the region 0.3<x<0.4 being clearly due to the orbit-width averaging, hence smoothing, of the peak $\nabla T_i(x)$ across the ITB foot.

Figures 19(a) and 19(b) show the temporal evolution of $E_r(x,t)$ and its components at t=6.1sec and R=3.35m, around the time/foot of the ITB: we note the slow build-up of the toroidal component due to an improved confinement after t=6.2sec. Note the importance of a slightly different ion density profile when comparing the pressure gradient component of $E_r(x,t)$ as calculated using E-field and E-JETTO: the factor ~3 difference in $\nabla p_D/n_D$ around the foot of the ITB around t=6sec is solely due to the apparently minor differences in $n_D(x,t)$ shown in Fig.18(a)/(b), since care was taken to use in E-field the same numerical scheme used in JETTO//NCLASS to compute the gradients (3-points derivative with no additional smoothing). The effect of the orbit width averaging (evaluated using a weighted combination of banana and potato orbits as indicated above) is clear in smoothing out the various gradients determining the poloidal and pressure components of $E_r(x,t)$ around the foot of the ITB, hence affecting the balance between $\nabla p/n$ and $V_\theta \times B_\phi$. This can change (as demonstrated here) the ExB shearing rate at the foot of the ITB because of the different ∇p, V_θ and V_ϕ profiles, with implications for theories and modelling (see for instance Refs.[4] and the further references therein) that associate improved confinement in ITB plasmas to turbulence suppression via the ExB shear.

C) ITB PLASMAS: HIGH PERFORMANCE ITB WITH SMALL POTATO ORBITS.

As a second example of high performance ITB plasmas with large ∇T_i, we now turn our attention to Pulse No: 58094. This pulse differs from Pulse No: 61349 in that the q-profile is much flatter, with a lower q_{MIN}. Hence potato orbits are smaller, and there are less of them in Pulse No: 58094 than Pulse No: 61349: as an example, $\delta_{ORB}\approx28$cm across the ITB location in Pulse No: 61349, whereas it is only $\delta_{ORB}\approx17$cm in Pulse No: 58094. Figure 20 shows the main plasma parameter for this pulse: here $\rho_{\theta D}(x,t)=O(L_{pD}(x,t))$ for x<0.2, the ITB is formed at t=6.5sec around x=0.45, and the plasma later disrupts at t=6.9sec. Figures 21(a) and 21(b) show the main plasma and collisionality parameters at t=6.6sec and R=3.48m, the position of the foot of the ITB, respectively. Here the profiles were computed using spline fit, $n_D(x)$ was obtained from the measured $n_C(x)$ and $n_e(x)$ using local charge neutrality. Figures 22(a) and 22(b) show the components of the calculated $E_r(x,t)$

20

at t=6.6sec and R=3.48m, respectively: we note again the clear smoothing of the $\nabla p/n$ and $V_\theta \times B_\phi$ components due to the averaging over the ion orbit width. However, the effect is much smaller that in Pulse No: 61349, and this is more clearly elucidated comparing the E_{rC}/ρ_{DEP} profile, shown in Fig.23(a) and Fig.23(b) for Pulse No: 61349 and Pulse No: 58094, respectively. In both these plots the black vertical line around x=0.2 indicate the boundary region for the validity of the neoclassical calculation, since $\rho_{\theta D}(x,t)=O(L_{pD}(x,t))$ for x<0.2. On the other hand, the use of the $\rho_{DEP}(x,t)$ normalisation of $E_r(x,t)$ improves significantly the accuracy of the results for x>0.8, since $E_r(x,t)$ and $\rho_{DEP}(x,t)$ have a very similar dependency on the density and Z_{EFF} edge value. We clearly notice the sudden drop and then overall increase and broadening of the E_r profile at the ITB onset for Pulse No: 61349: due to the very large ion orbit width, $E_r(x,t)$ is also very flat in this case across the main part of the poloidal cross section. We also notice that the region of large radial electric field extends progressively towards the plasma boundary as the steady-state ITB develops in time. On the other hand, due to the much smaller ion orbit width, we notice that the E_r/ρ_{DEP} profile is much more peaked in Pulse: 58094, and that the edge region x>0.8 remain characterised by values of $E_r(x,t)$ hovering around $E_r(x,t)=0$ as the ITB develops during the steady-state heating phase. The two clear drops in the E_{rC}/ρ_{DEP} profile for Pulse: 58094 at t=4.0sec and t=5.0sec are linked to the appearance of the q=3 and q=5/2 surfaces around mid-radius, similarly to Pulse No: 61349 just at the time of ITB onset. The ITB target q-value is the q=2 surface appearing around mid-radius at t=6.0sec: this however is not associated to any change in the E_{rC}/ρ_{DEP} because the ITB onset, increasing $E_r(x=0.5)$ compensate the drop caused by the appearance of a low-order rational q-surface. These observations then link empirically the appearance of low-order rational q-surfaces to rapid transient changes in the E_r profile, and are as well in many aspects reminiscent of the proposed *q-comb* model for the transport coefficients [25], which has recently been applied to JET data [26].

D) L-MODE, H-MODE AND ITB PLASMAS.

In this last Section we review and summarise the results we have obtained for the calculated $E_r(x,t)$ during steady-state L-mode (Pulse No: 58263, t=20.0sec), H-mode (Pulse No: 57819, t=8.0sec) and ITB (Pulse No: 58094, t=6.6sec) phases. Figure 24(a) shows the input plasma data and computed neoclassical collisionality factors for the three pulses and time slices indicated above, and Fig.24(b) shows the computed E_{rC}/ρ_{DEP}. The background plasma data used for this calculation were processed using spline fitting, $n_D(x)$ was computed from the measured $n_C(x)$ and $n_e(x)$ profiles using local charge neutrality (no normalisation using Z_{EFF} from Bremsstrahlung), and averaging over the ion orbit width. It is immediate to note the striking similarity in the shape of the normalised E_r/ρ_{DEP} profile between the L-mode and ITB cases in the plasma core, up to around mid-radius. The H-mode radial electric field is definitively negative for x>0.85, hovering around $E_r(x,t)=0$ for L-mode plasmas, and positive for ITB plasmas, although in this case there are very significant error bars. This comparison clearly demonstrates that for a moderately reversed q-profile, where very large potato orbits constitute only a minor fraction of the trapped ion orbits, the ExB shear does indeed becomes an important ingredient in generating and sustaining the ITB through turbulence suppression.

CONCLUSIONS

In this work we have presented a complete evaluation of the uncertainties affecting the neoclassical calculation of the radial electric field in JET plasmas, using a comparison between transport codes such as JETTO and NCLASS and an analytical approximation that specifically includes the basic features of the JET geometry (plasma elongation, flux-surface averaging) and magnetic equilibrium (non-monotonic q-profile leading to non-standard orbits such as the potato ones). Starting from the absolute calibration of the core CX system, we developed an analytical formulation for the error bar on the calculated $E_r(x,t)$, which allows us to consistently assess if different numerical and modelling approaches can lead to significant differences in $E_r(x,t)$, i.e. exceeding the expected uncertainty.

First, the inconsistency intrinsic to the neoclassical theory developed in Ref.[7], i.e. the assumption of a plasma made up only of electrons, one main and one impurity ion species, may lead to serious discrepancies in the calculated $E_r(x,t)$ when using Z_{EFF} from Bremsstrahlung as a constraint to normalise the ion density profiles. Second, care should be taken when considering averaging over the ion orbit motion: for the typical case of a monotonic q-profile with $q_0 \sim 1$, we have demonstrated that such averaging over the ion banana orbit does not modify the resulting $Er(x,t)$. On the other hand, significant differences arise in ITB plasmas with a deeply non-monotonic q-profile ($q_0 > 5$, $q_{MIN} \sim 2-3$) when large potato orbits are present and need to be considered for averaging $E_r(x,t)$.

A question mark on the validity of the neoclassical calculation of $E_r(x,t)$ remains, since it has not been clearly demonstrated whether the poloidal velocity is indeed neoclassical or anomalous. The neoclassical calculations used in this work demonstrate that in certain experimental conditions $|V_\theta / V_\phi| \approx O(|B_\theta / B_\phi|)$. As an example of this, the poloidal component of $E_r(x,t)$ becomes important around the ITB location region due to a non-exact cancellation between the $\nabla p/n$ and the $V_\theta \times B_\phi$ components. At the plasma edge this situation is further complicated by the significant reduction in the toroidal velocity due to lower momentum input, which in some cases casts some doubts on the sign of $E_r(x,t)$ at the edge pedestal.

Moving now onto the physics results, we demonstrated a striking similarity in the shape of $E_r(x,t)$ in L-mode and ITB plasmas (with a flat q-profile and $q_0 \sim q_{MIN} \sim 2$) in the plasma core and towards the plasma boundary, although in this region uncertainties in the Z_{EFF} and density profile and the lack of V_θ measurements (or a convincing experimental validation of the predicted neoclassical value) prevent a more detailed analysis. This demonstrates as well that when large potato orbits are not dominant, indeed the ExB shearing rate can play a significant role in generating and sustaining the transition to higher-confinement regimes through turbulence suppression. We also demonstrated the role of prompt NBI losses when comparing H-mode plasmas with forward and reversed ion ∇B-drift direction: the larger the plasma current in RBE pulses, the better the confinement of NBI ions, the closer is the shape of the edge $E_r(x,t)$ to that typical for the FBE case.

ACKNOWLEDGEMENTS

22

REFERENCES

[1]. F. Levington et al., Phys. Rev. Lett. 75, 4417 (1995).

[2]. C. Challis et al., Plasma Phys. Control. Fusion **43**, 861 (2001).

[3]. F. Wagner et al., Phys. Rev. Lett. **49** 1408, (1982).

[4]. D. Ward, Plasma Phys. Control. Fusion **38**, 1201 (1996); M.Tendler, Plasma Phys. Control. Fusion **39**, B371 (1997); K.Burrell, Phys. Plasmas **4**, 1499 (1997).

[5]. J. Wesson, Tokamaks, 3rd edition, (Oxford Science Publication, Oxford, 2003), p.617.

[6]. N. Hawkes et al., Plasma Phys. Control. Fusion **38**, 1261 (1996).

[7]. S. Hirshman and D.Sigmar, Nucl. Fus. **21**, 1079 (1981).

[8]. Y. Kim et al., Phys. Fluids B3, 2050 (1991).

[9]. D. Testa et al., Phys. Plasmas **9**, 243 (2002).

[10]. C. Giroud et al., Calibration and alignment technique of the core charge-exchange diagnostic at JET, to be submitted to Review of Scientific Instruments, December 2004.

[11]. G. Cenacchi and A. Taroni, JETTO: a free-boundary plasma transport code, Report ENEA-RT-T113-88-5, Centro Ricerche Energia, Bologna, Italy, 1988.

[12]. W.Houlberg et al., Phys. Plasmas **4**, 3230 (1997).

[13]. K. Shaing et al., Phys. Fluids B4, 2547 (1992); K.Shaing et al., Phys. Plasmas 1, 3365 (1994).

[14]. C. Angioni and O. Sauter, Phys. Plasmas **7**, 1224 (2000).

[15]. M. Tokar, Plasma Phys. Control. Fusion **45**, 1323 (2003).

[16]. J. Wesson, Tokamaks, 3rd edition (Oxford Science Publication, Oxford, UK, 1997), p.665.

[17]. J. Kim et al., Phys. Rev. Lett. 72, 2199 (1994).

[18]. V. Merezhkin, Soviet JETP 4, 152 (1978).

[19]. D. Testa et al., Review of Scient. Instrum. **74**, 1694 (2003).

[20]. L.-G. Eriksson and F. Porcelli, Plasma Phys. Control. Fusion **43**, R145 (2001).

[21]. P. Stubberfield and M.Watkins, Multiple PENCIL Beam, JET-DPA(06)/87, 1987.

[22]. D. Testa at al., Phys. Plasmas 6 (1999), 3498; D.Testa at al., Phys. Plasmas **6** (1999), 3489.

[23]. W. Suttrop et al., Plasma Phys. Control. Fusion **39**, 2051 (1997).

[24]. Y. Andrew et al., Plasma Phys. Control. Fusion **46**, 337 (2004).

[25]. M.de Baar et al., Phys. Plasmas **6** (1999), 4645; G. Hogeweij et al., Nucl .Fus. **38** (1998), 1881.

[26]. M.de Baar and G. Hogeweij, private communications, JET Facilities, 2004.
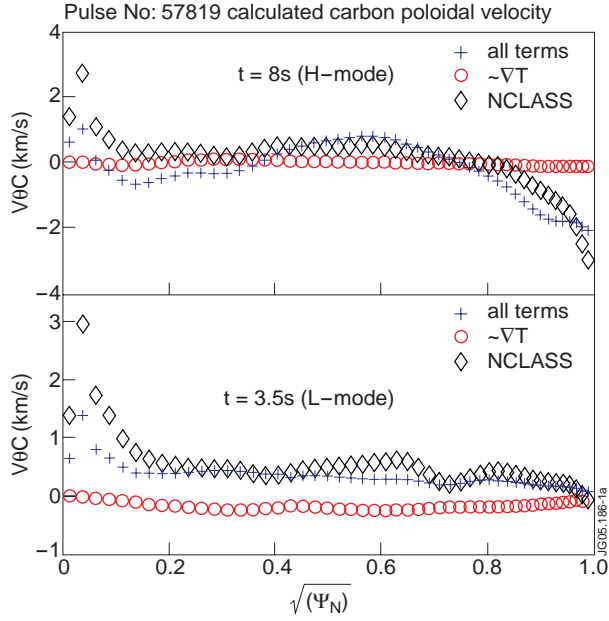
Figure 1(a): The carbon poloidal velocity $V_{\theta C}$ calculated with NCLASS and using Eq.8,9(a) for the L- and H-mode phases of Pulse No: 57819, showing good agreement in the region $0.3<x<0.8$ between NCLASS and the full analytic approximation of Eq.8.
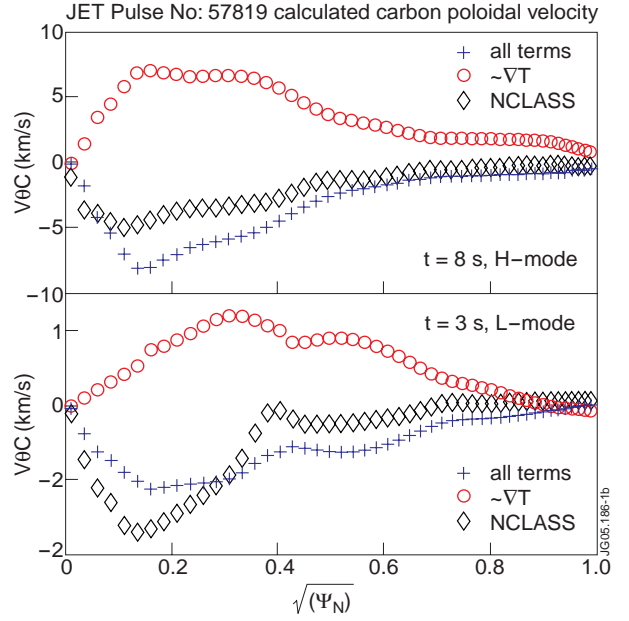
Figure 1(b): The deuterium poloidal velocity $V_{\theta D}$ calculated with NCLASS and using Eqs.8,9(a) for the L- and H-mode phases of Pulse No: 57819, showing good agreement in the region $0.2<x<0.9$ between NCLASS and the full analytic approximation of Eq.8, particularly during the H-mode phase.
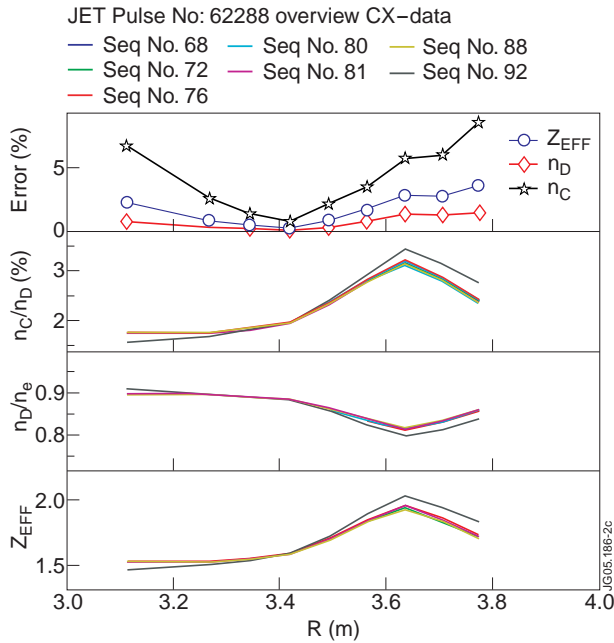
Figure 2: Systematic errors in the CX measurements of n_C, n_D and Z_{EFF} for one of the reference calibration pulses: the various labels in the legend indicate different methods for computing the CX active volume.
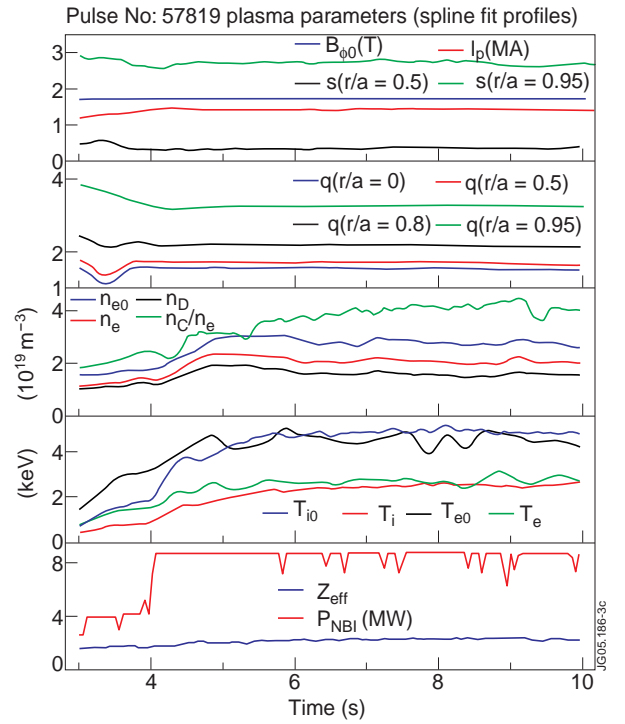
Figure 3: Main plasma parameters for Pulse No: 57819: here $<X>$ indicates a volume-averaged value, and $s=(r/q)(dq/dr)$ is the shear in the safety factor profile.
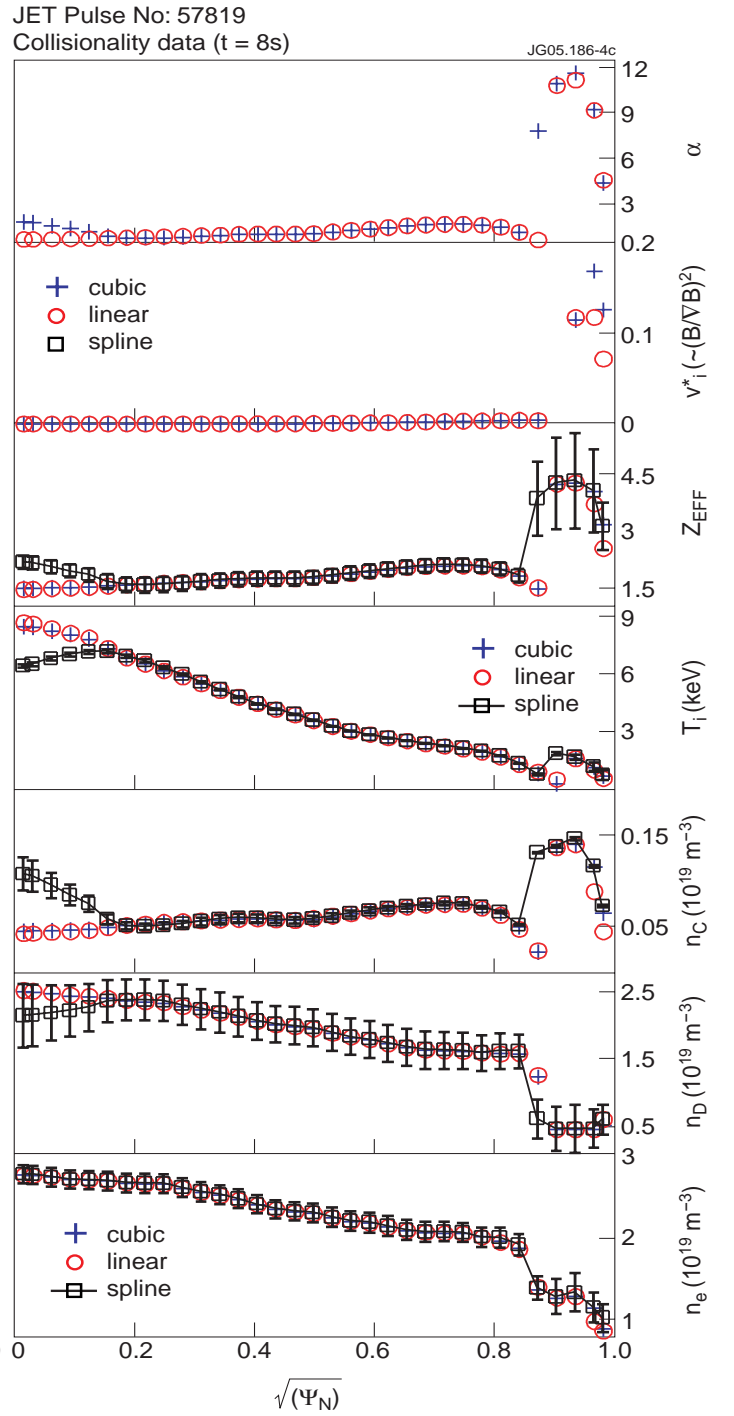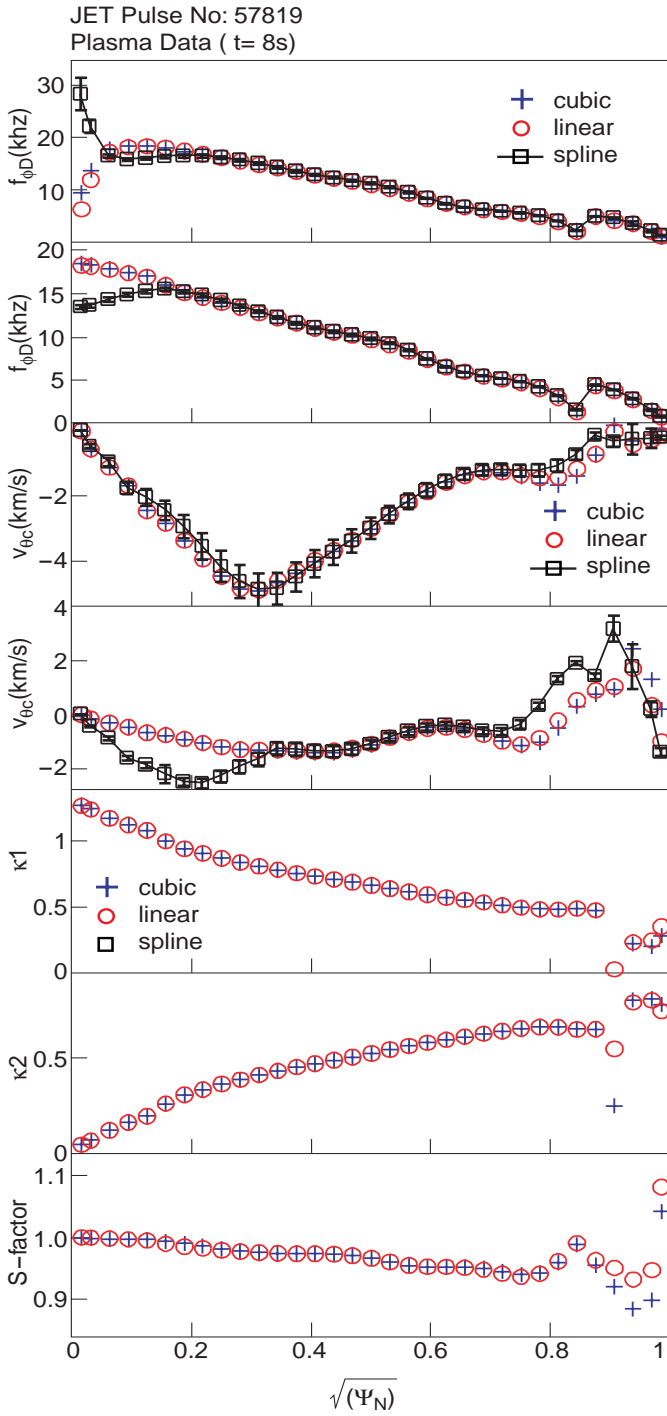
Figure 4: Various input plasma data and neoclassical collisionality factors computed using spline, linear and cubic fitting routines for the H-mode phase of Pulse No: 57819: note the differences between these three methods when extrapolating towards the magnetic axis (R_0=2.98m) and the plasma boundary (R=3.92m) the CX data, which are directly measured only in the region 3.15<R(m)<3.8.
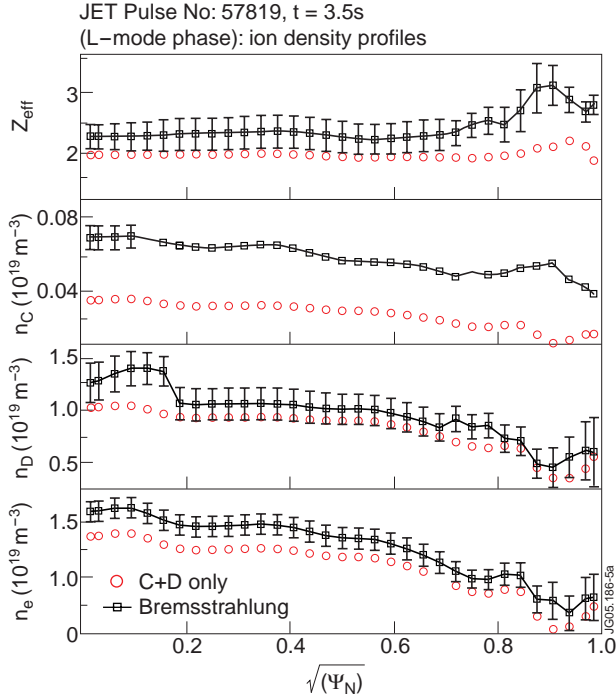
Figure 5(a): Comparison between the deuterium and carbon density profiles obtained with/out Z_{EFF}-normalisation from Bremsstrahlung for the L-mode phase of Pulse No: 57819, which clearly illustrates the differences in the resulting n_C and n_D profiles.
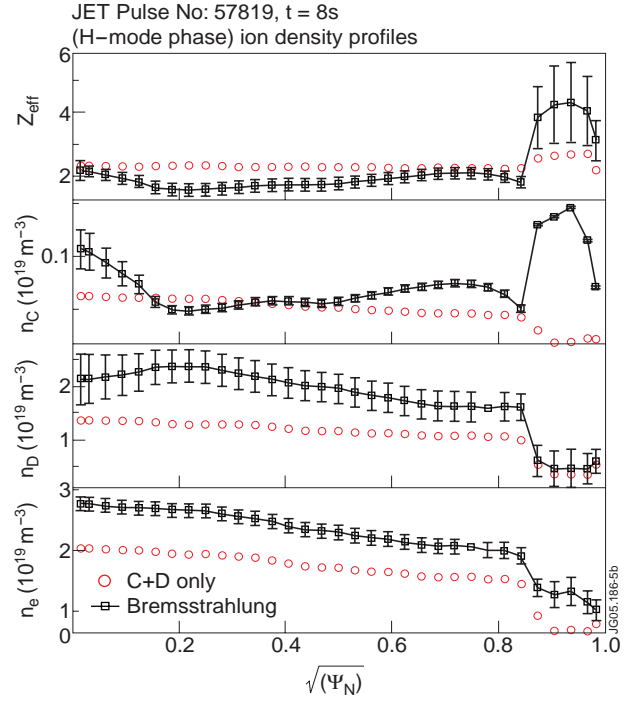
Figure 5(b): Comparison between the deuterium and carbon density profiles obtained with/out Z_{EFF}-normalisation from Bremsstrahlung for the H-mode phase of Pulse No: 57819, which clearly illustrates the differences in the resulting n_C and n_D profiles.
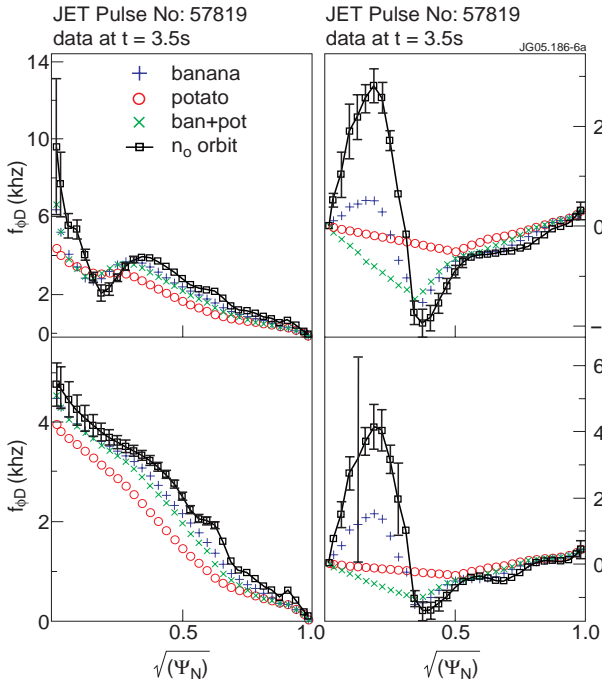
Figure 6(a): Effect of orbit-width averaging on the computed poloidal rotation velocity and toroidal rotation frequency profiles during the L-mode phase of Pulse No: 57819: note the clear smoothing of the double-hump structure in $V_{\theta C}$ and $V_{\theta D}$ in the plasma core, for $0.2 < x < 0.4$.
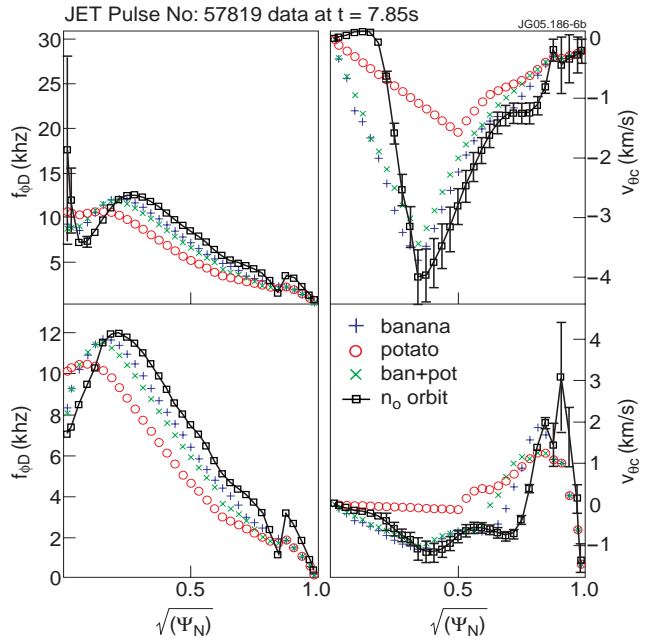
Figure 6(b): Effect of orbit-width averaging on the computed poloidal rotation velocity and toroidal rotation frequency profiles during the H-mode phase of Pulse No: 57819: note the smoothing of the peaks in $V_{\theta C}$ (at the plasma edge) and $V_{\theta D}$ (towards mid-radius), and the slight inward shift of the profiles.

26
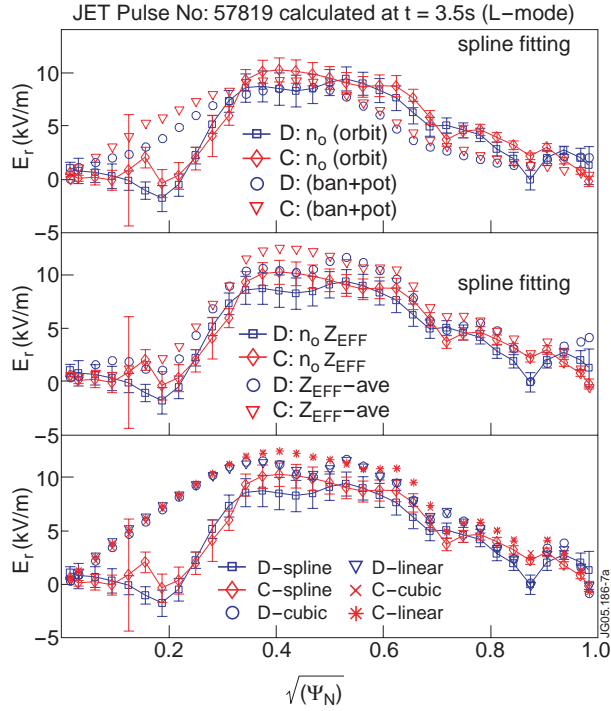
Figure 7(a): The effect of the various numerical schemes used by E-field to calculate E_r for Pulse No: 57819 at t=3.5sec, during the L-mode phase. Note the clear effect in the plasma core of the different numerical routines used for inter/extrapolating.
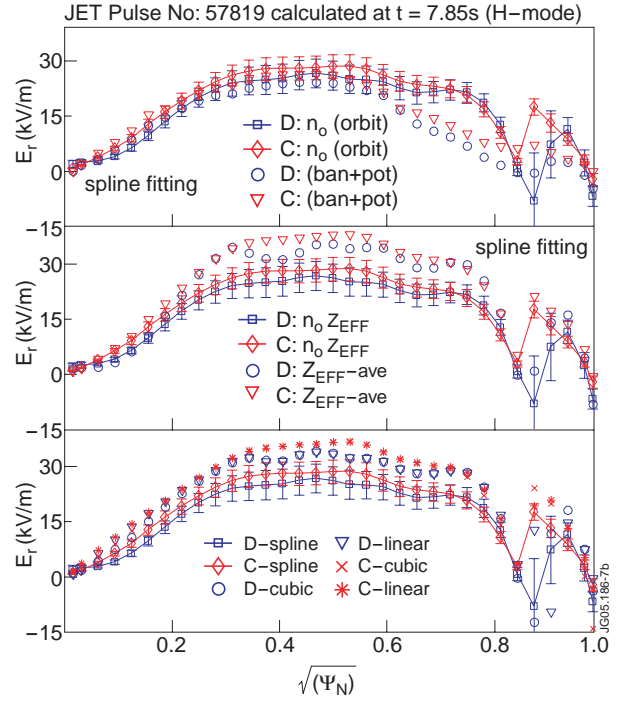
Figure 7(b): The effect of the various numerical schemes used by E-field to calculate E_r for Pulse No: 57819 at t=7.85sec, during the steady-state H-mode phase. We notice however the different sign of E_r at the top of the pedestal, for $0.8<x<0.9$, which is due to a non-exact cancellation between the pressure gradient and poloidal components of E_r.
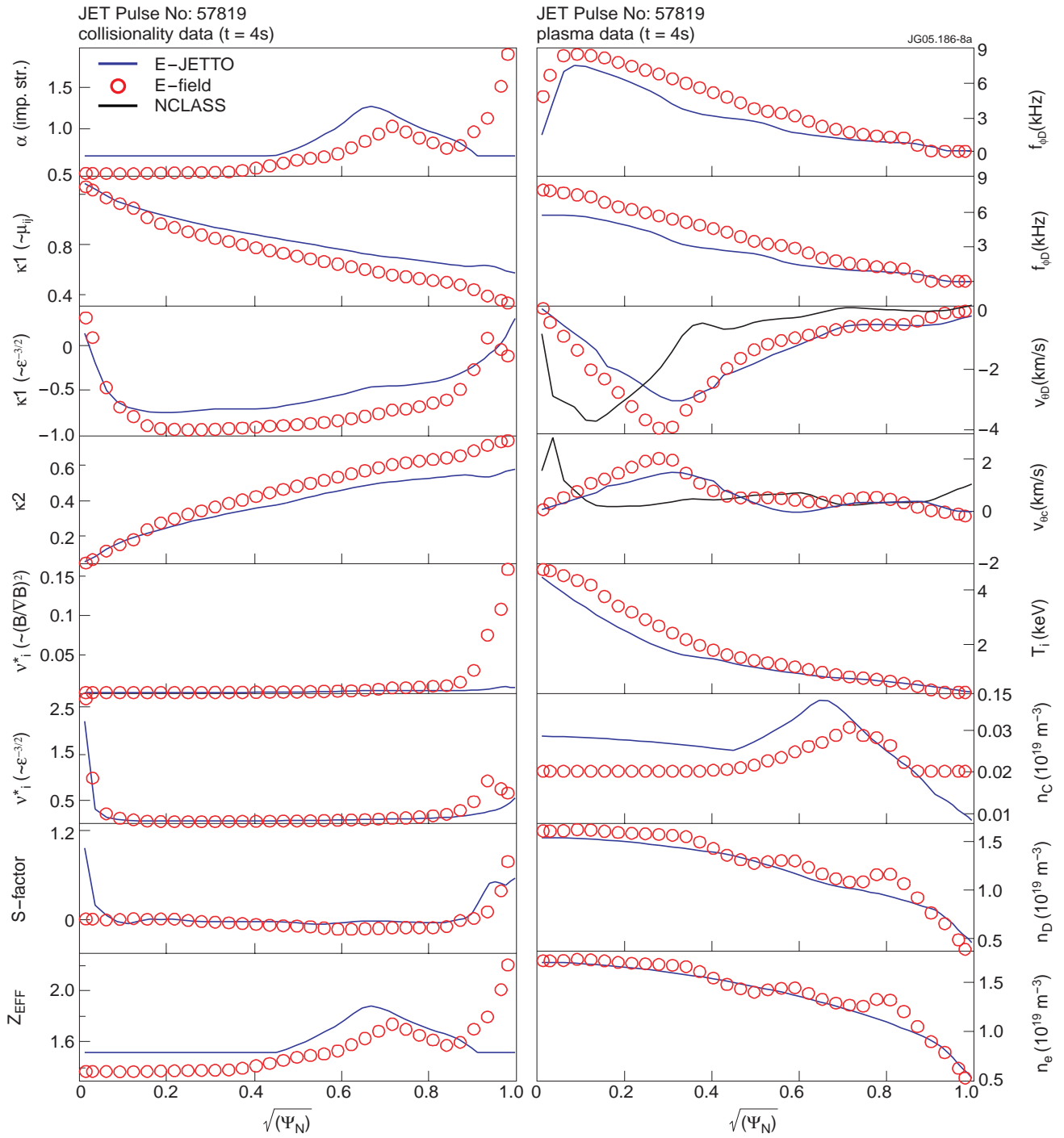
Figure 8(a): Plasma and neoclassical collisionality factors for the comparison between E_{rC} and E_{rD} calculated with NCLASS and E-field at t=4sec, during the steady-state L-mode phase.

28
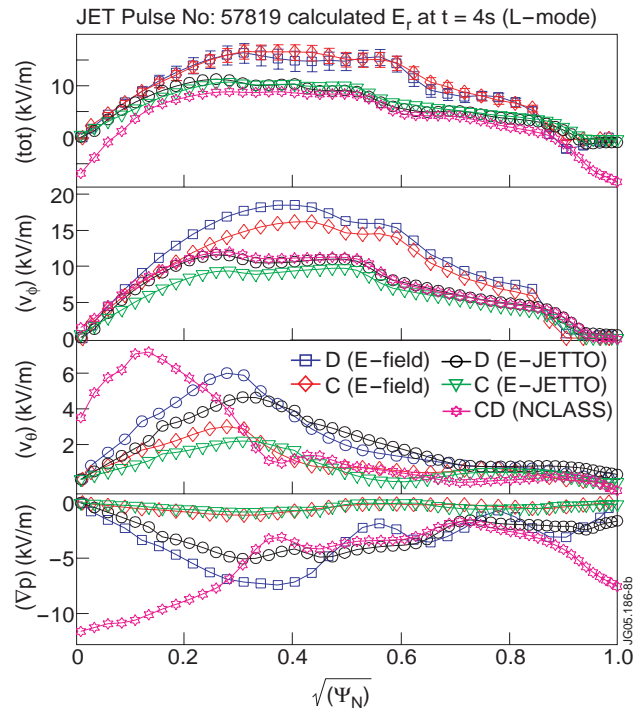
Figure 8(b): Comparison between the flux-surface averaged E_{rC} and E_{rD} calculated with NCLASS and E-field at t=4sec, during the steady-state L-mode phase. Note that discrepancy due to the different fitting of the measured $V_{\phi C}$ and Z_{EFF} profiles, particularly at the plasma edge and in the plasma core.
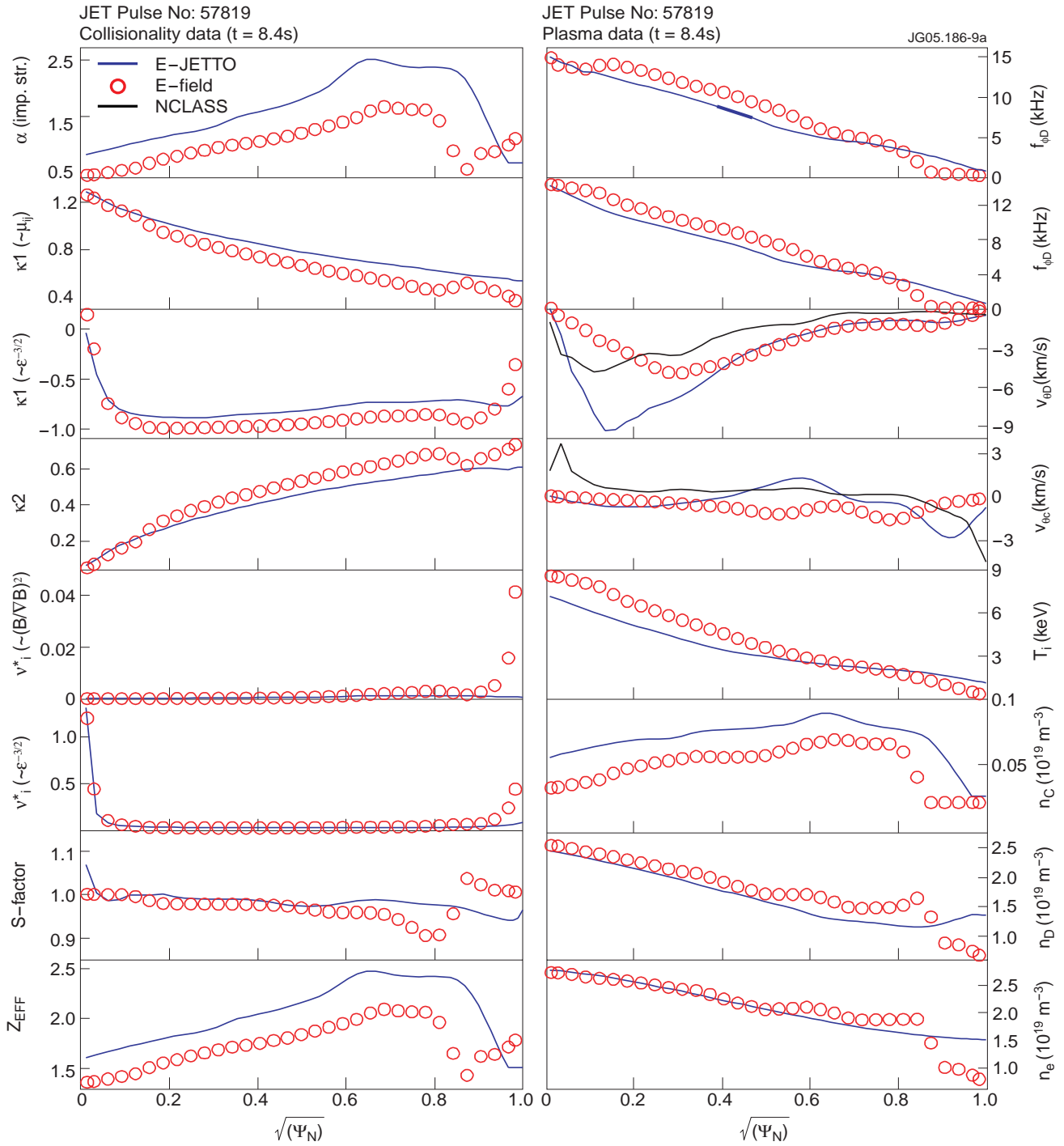
Figure 9(a): Plasma and neoclassical collisionality factors for the comparison between E_{rC} and E_{rD} calculated with NCLASS and E-field at t=8.4sec, during the steady-state H-mode phase.
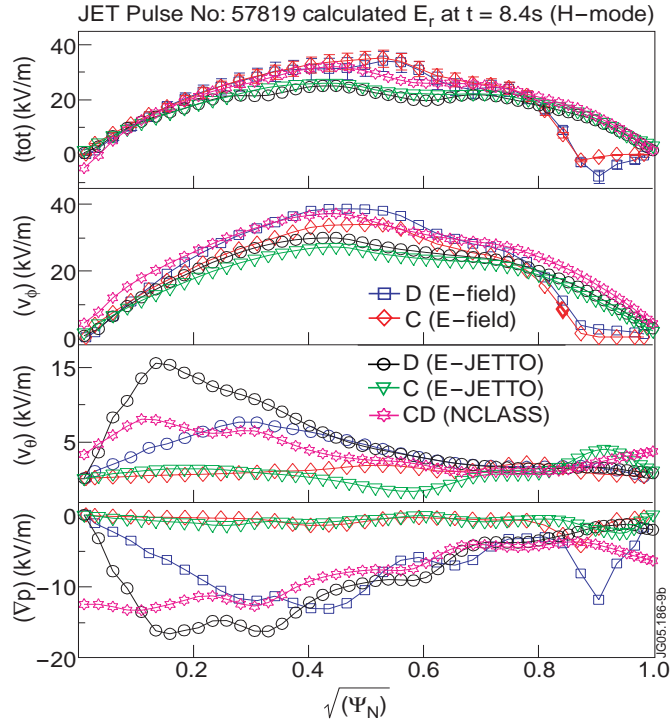
Figure 9(b): Comparison between E_r calculated with JETTO/NCLASS and E-field at t=8.4sec, during the steady-state H-mode phase: $<E_{r,CD}> \approx 10kV/m$ with NCLASS for $0.85<x<0.95$, but $E_r \approx 0$ with E-field, due to the different treatment of the edge pedestal in the measured n_e and $V_{\phi C}$ profiles.
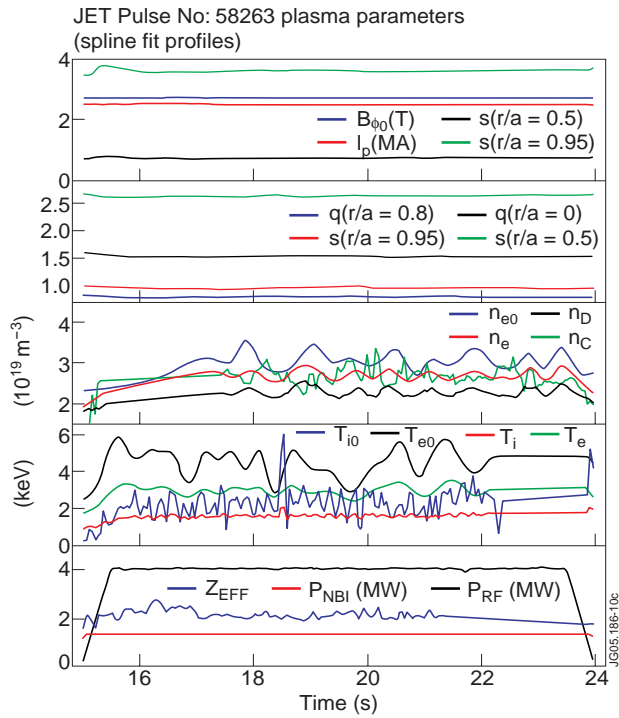
Figure 10: The main plasma parameters for Pulse No: 58263, a typical JET L-mode pulse.
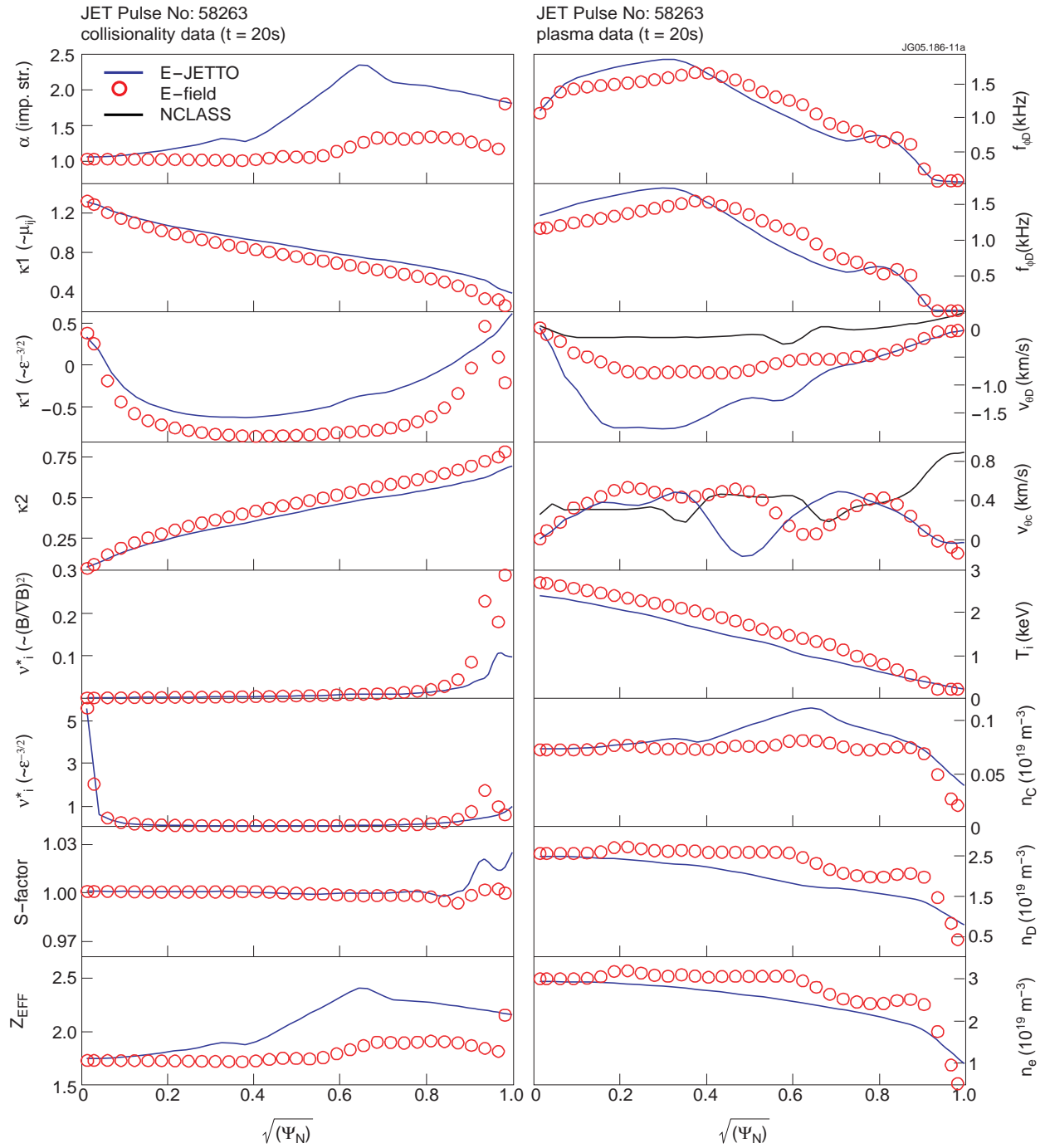
Figure 11(a): Plasma and neoclassical collisionality factors for the comparison between E_r calculated with NCLASS and E-field at t=20.0sec, during the steady-state L-mode phase.
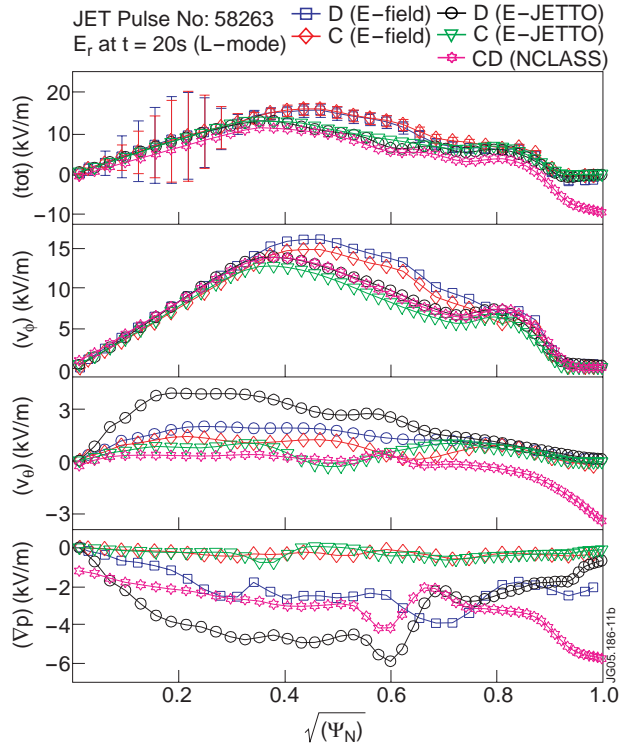
Figure 11(b): Comparison between E_r calculated with NCLASS and E-field at t=20.0sec, during the steady-state L-mode phase. For x>0.85 $V_\phi \times B_\theta \approx 0$ since $V_{\phi C} \approx V_{\phi D} \to 0$, and the balance between $\nabla p/n$ and $V_\theta \times B_\phi$ dominates E_r, whose value is thus largely affected by slightly different density profiles.
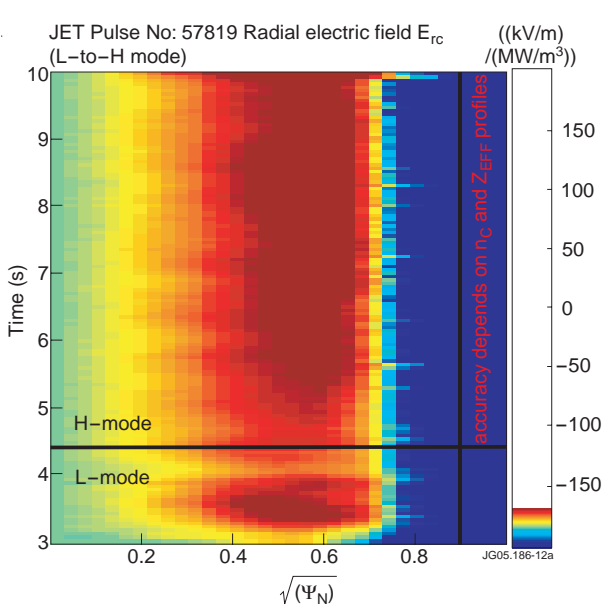
Figure 12(a): The 3D profile $E_{rC}(x,t)$ calculated with the E-field code for Pulse No: 57819, here normalised with respect to the total $P_{NBI}+P_{RF}$ power deposition profile. There is no significant difference around the edge pedestal at the L-H transition, whereas the transient drop in E_r around mid-radius is clearer.
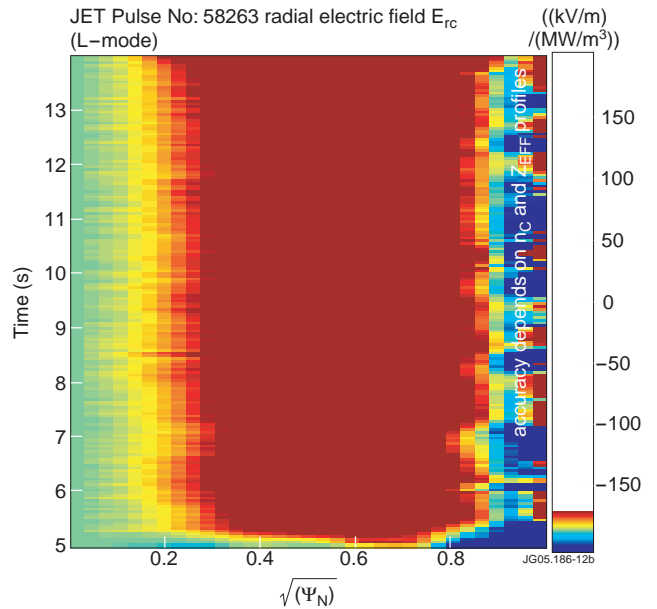
Figure 12(b): The 3D profile $E_rC(x,t)$ calculated with the E-field code for Pulse No: 58263, here normalised with respect to the total $P_{NBI}+P_{RF}$ power deposition profile. Note the broad and rather flat profile for 0.2<x<0.8, whereas the fine structures appearing for x>0.85 are not very reliable due to their strong dependence on the ion density and Z_{EFF} profiles used in the E_r calculation.

33
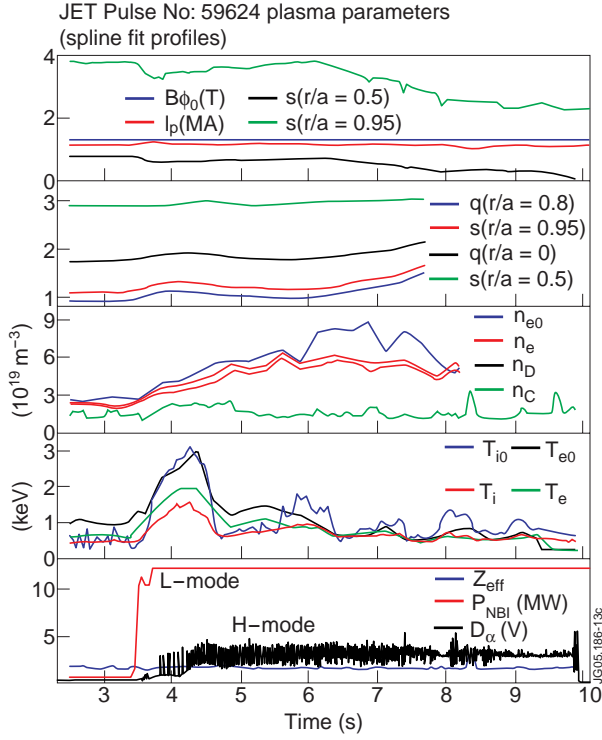
Figure 13: The main plasma parameters for Pulse No: 59624, a JET L-to-H-mode discharge with the ion ∇B-drift direction directed away from the strike points, contrary to the standard operating scenario.
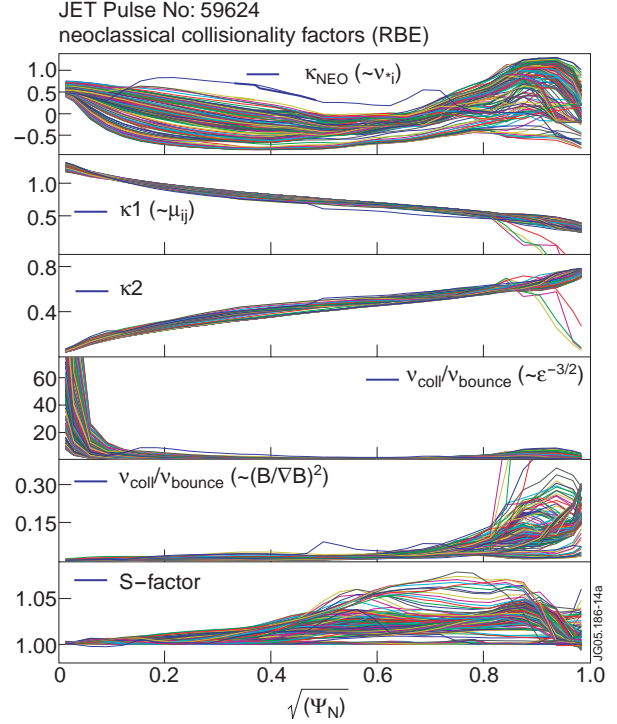
Figure 14(a): Neoclassical collisionality factors for Pulse No: 59624, the reversed ion ∇B-drift direction case.
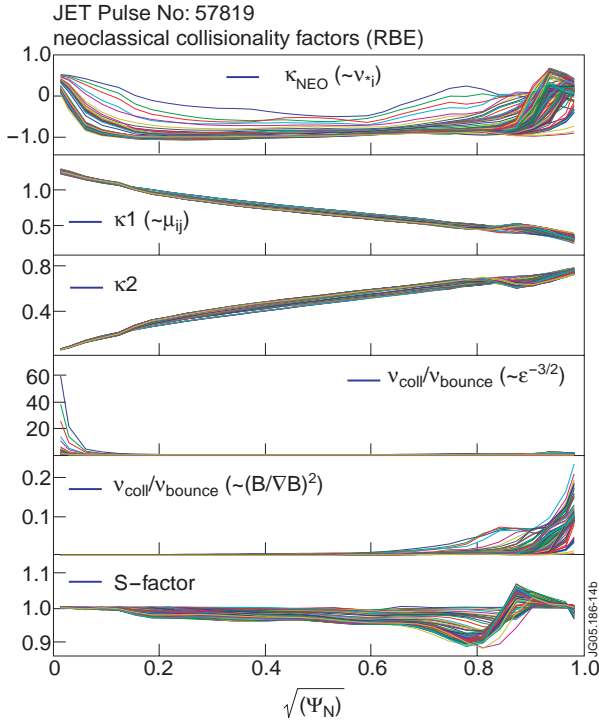
Figure 14(b): Neoclassical collisionality factors for Pulse No: 57819, the normal ion ∇B-drift direction case.
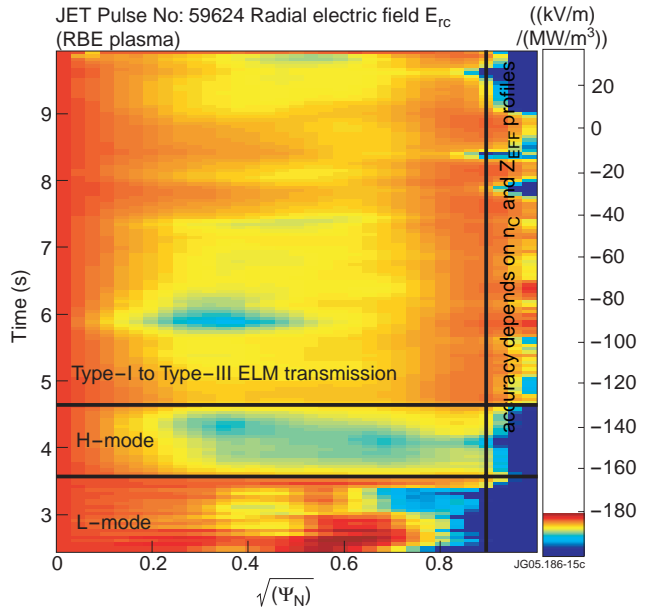
Figure 15: The 3D radial electric field for the reversed ion ∇B-drift direction pulse (No: 59624). Note that the change in the ELM behaviour at t=24.5sec, from Type-I to Type-III, only significantly affects the magnitude of E_r in the region 0.6<x<0.95 due to a change in the scale lengths, reducing its peaking but only marginally modifying its overall shape. In comparison with Fig.12(a), we immediately note here the different shape of E_r, particularly in the region 0<5<x<0.9.
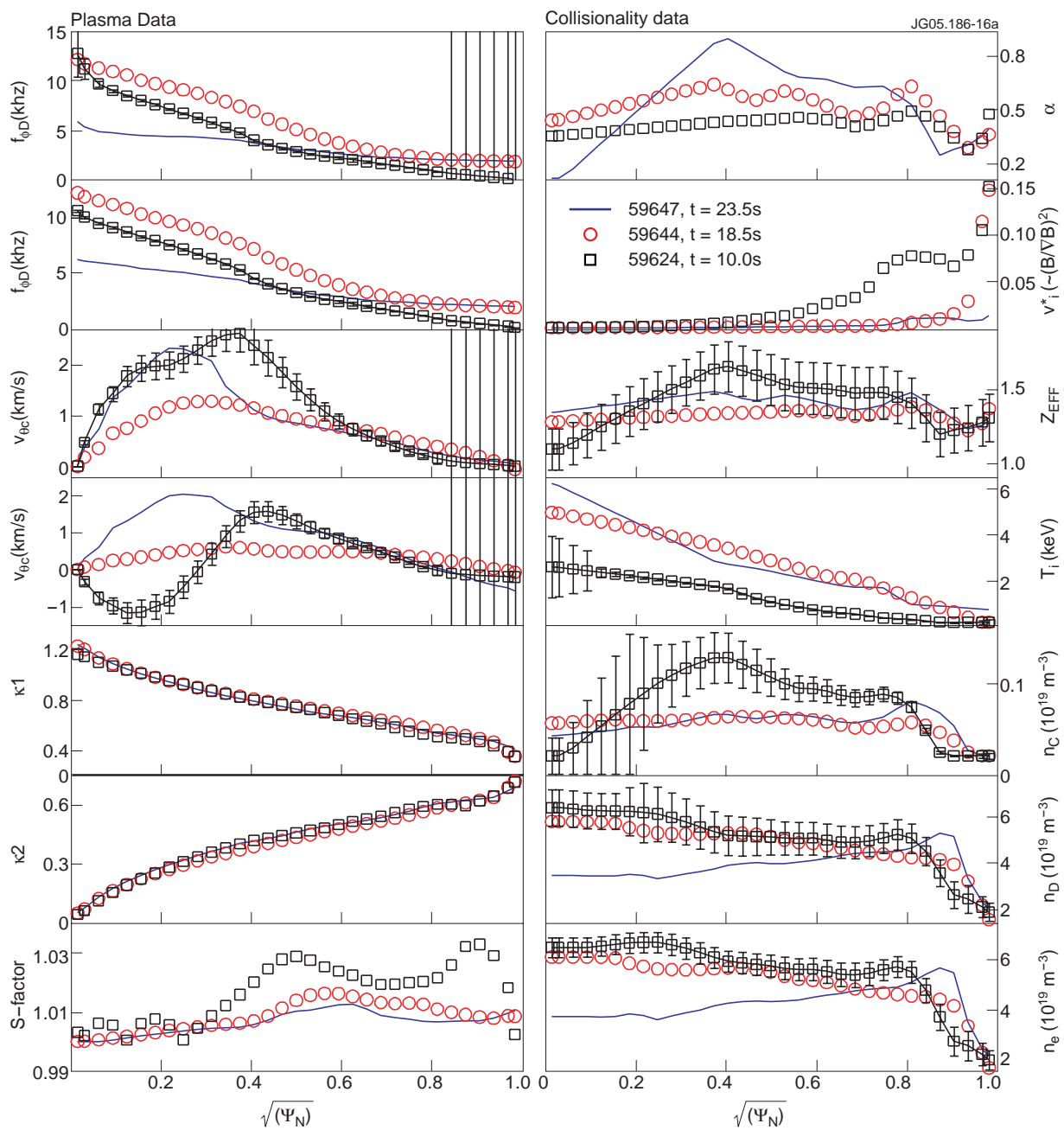
Figure 16(a): Plasma and neoclassical collisionality factors for the E_r comparison between reversed ion ∇B-drift discharges with different values of the plasma current.
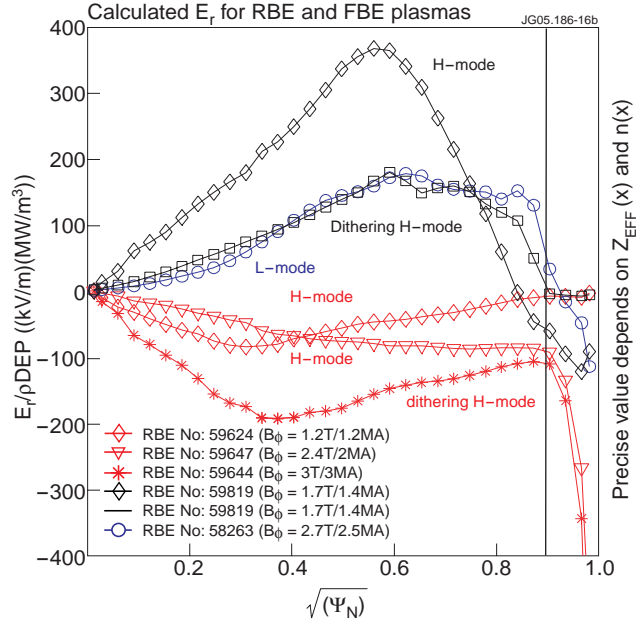
Figure 16(b): The calculated radial electric field for the three RBE and the reference FBE pulses, normalised with respect to the input $\rho_{DEP}(x)$. We notice clear differences in the $E_r(x)$ profile, both in shape and magnitude: in particular, the FBE pulse at higher plasma current (Pulse No: 59644) has the $E_r(x)$ more closely resembling that of the reference H-mode pulse, thus empirically confirming the role of NBI losses at the plasma edge in determining $E_r(x,t)$.
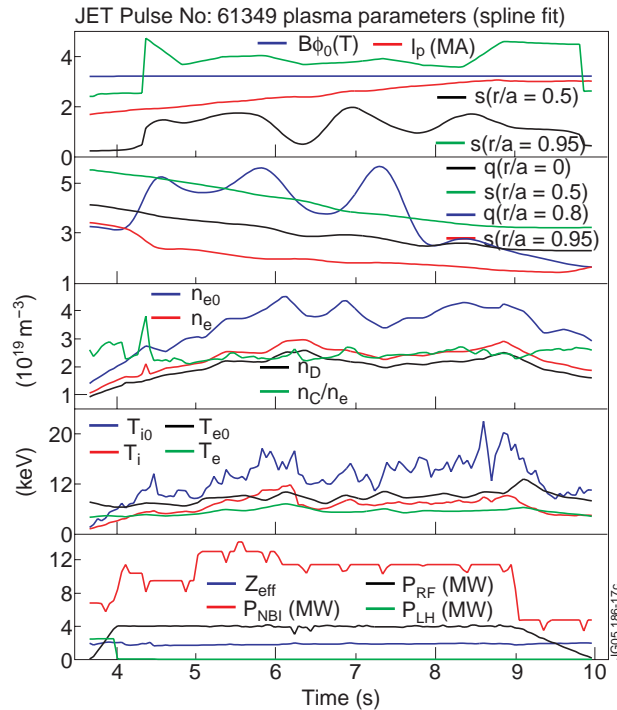
Figure 17: The main plasma parameters for Pulse No: 61349, an ITB pulse with a deeply non-monotonic q-profile where ∇T_i reaches the value of ~250keV/m around R=3.35m, across the ITB position.
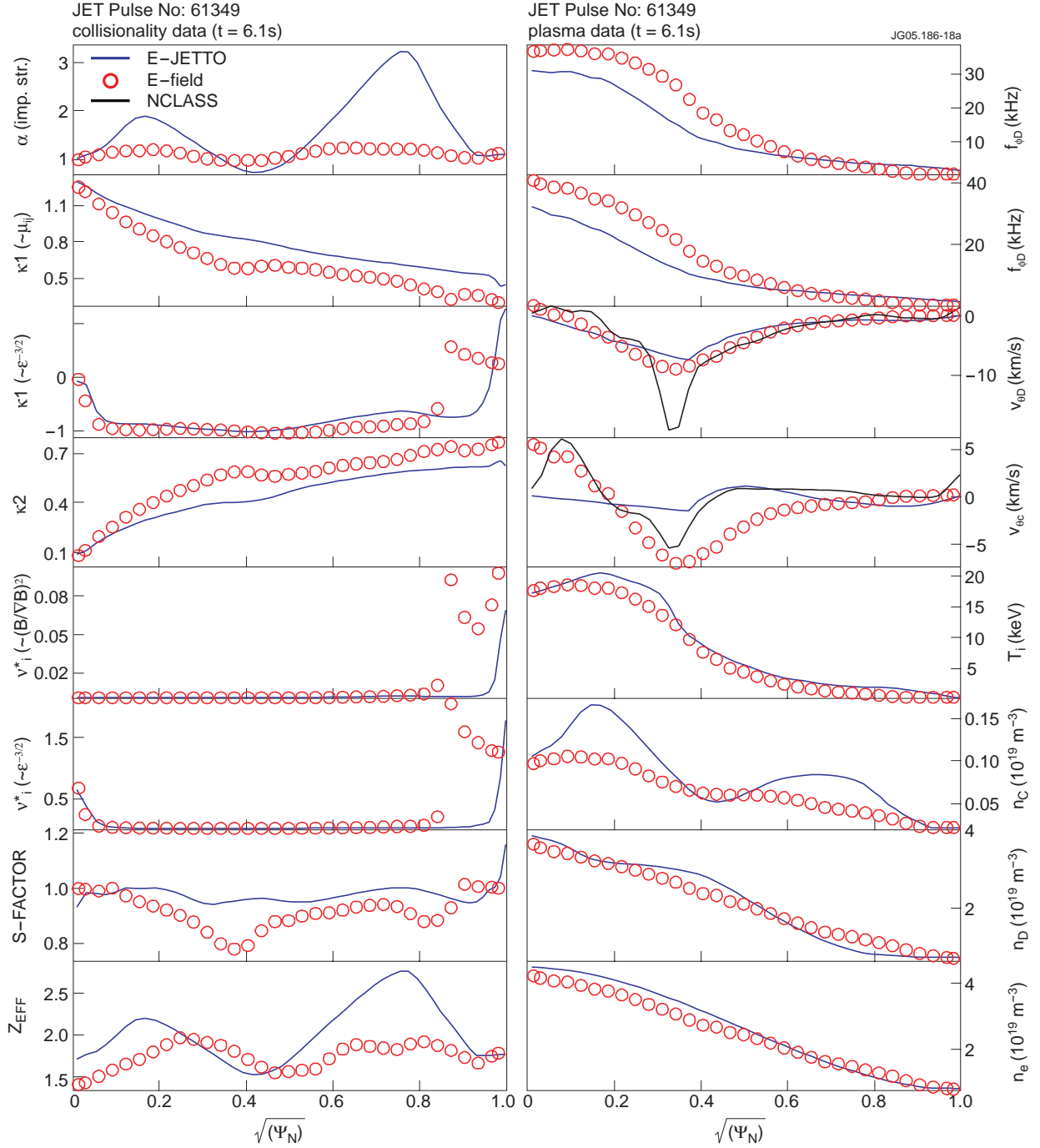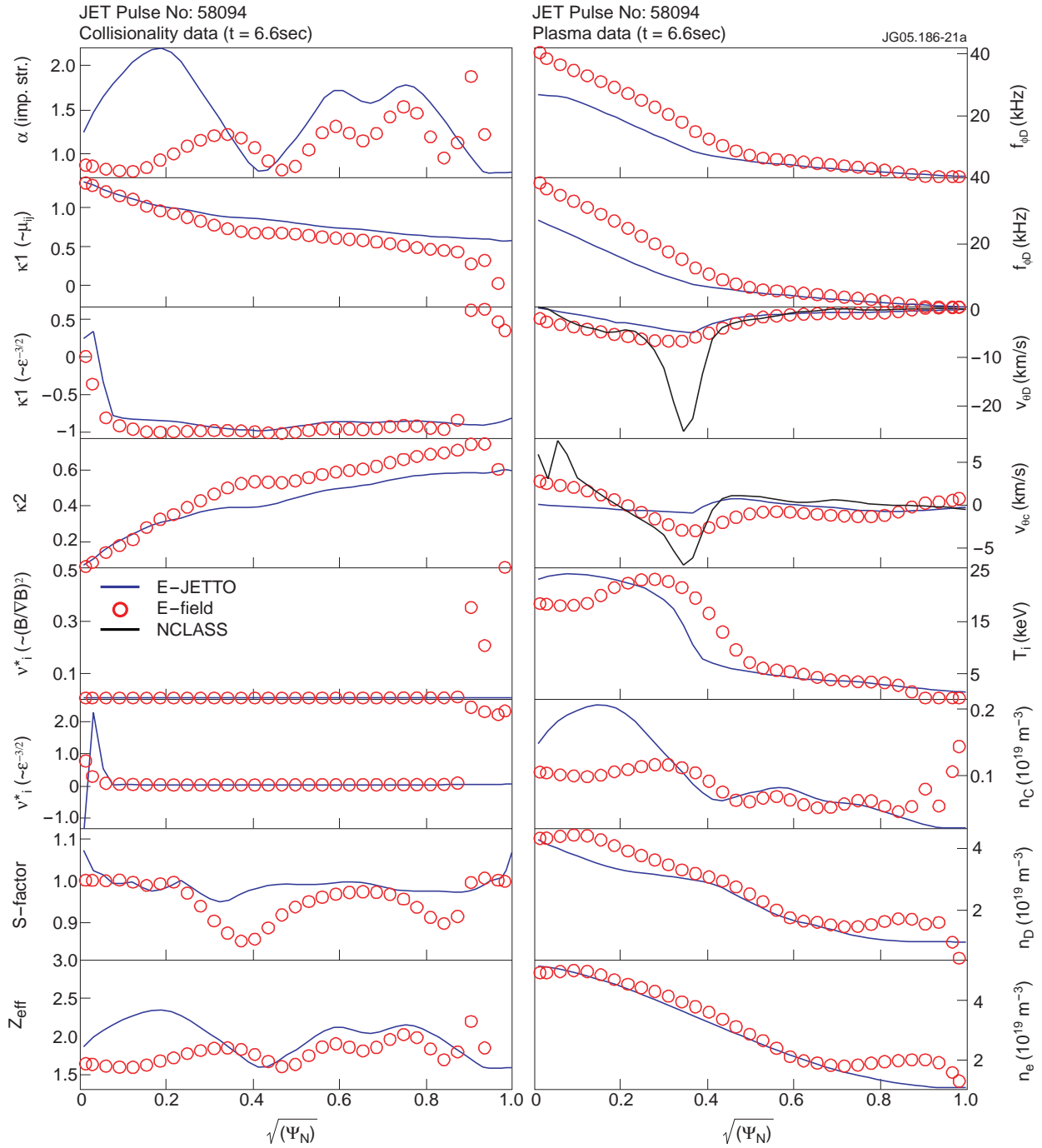
Figure 18(a): Plasma and neoclassical collisionality factors for the E_r comparison between E-field and NCLASS for the ITB Pulse No: 61349, at t=6.1, the time of the peak $T_i(x,t)$.
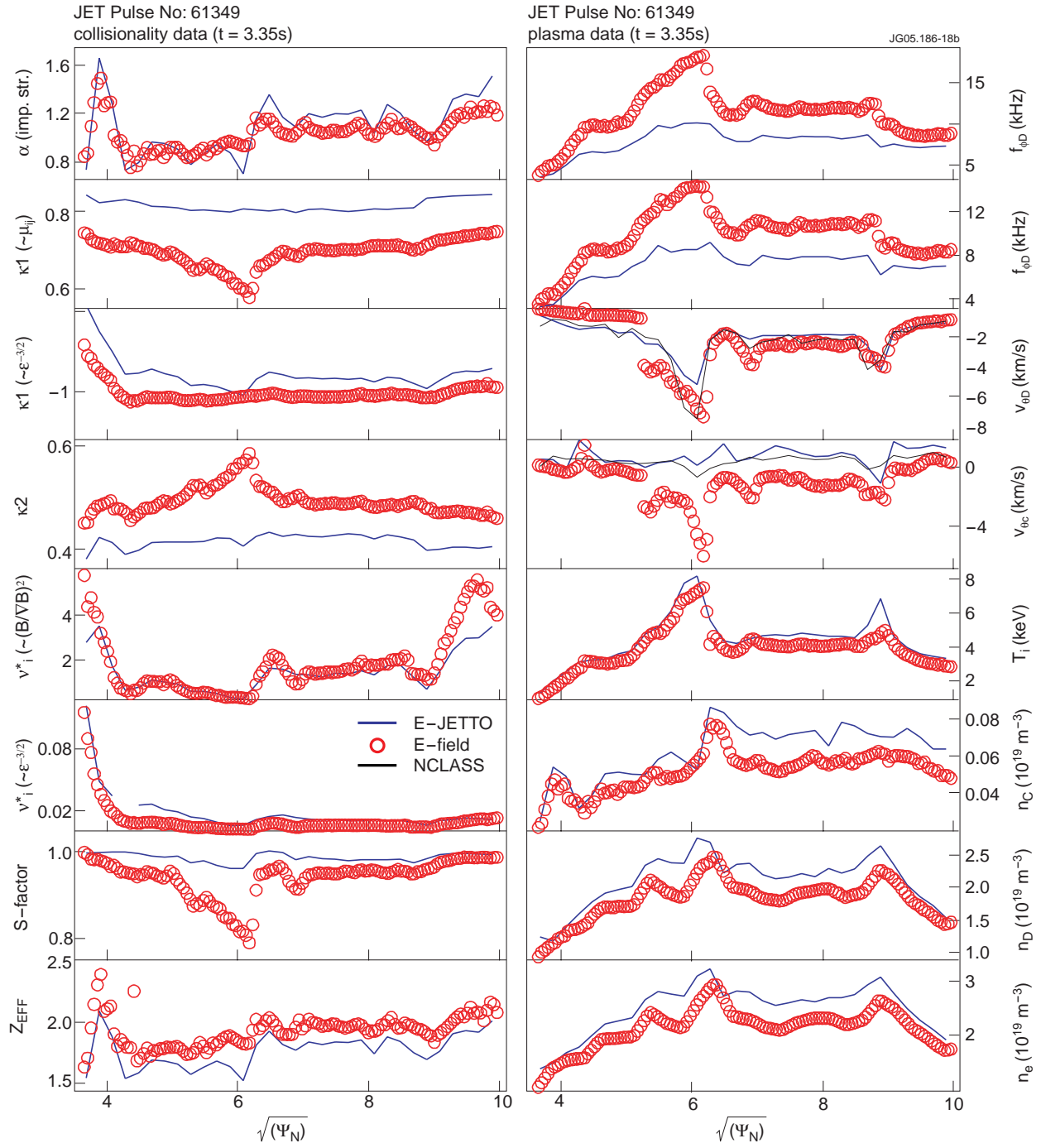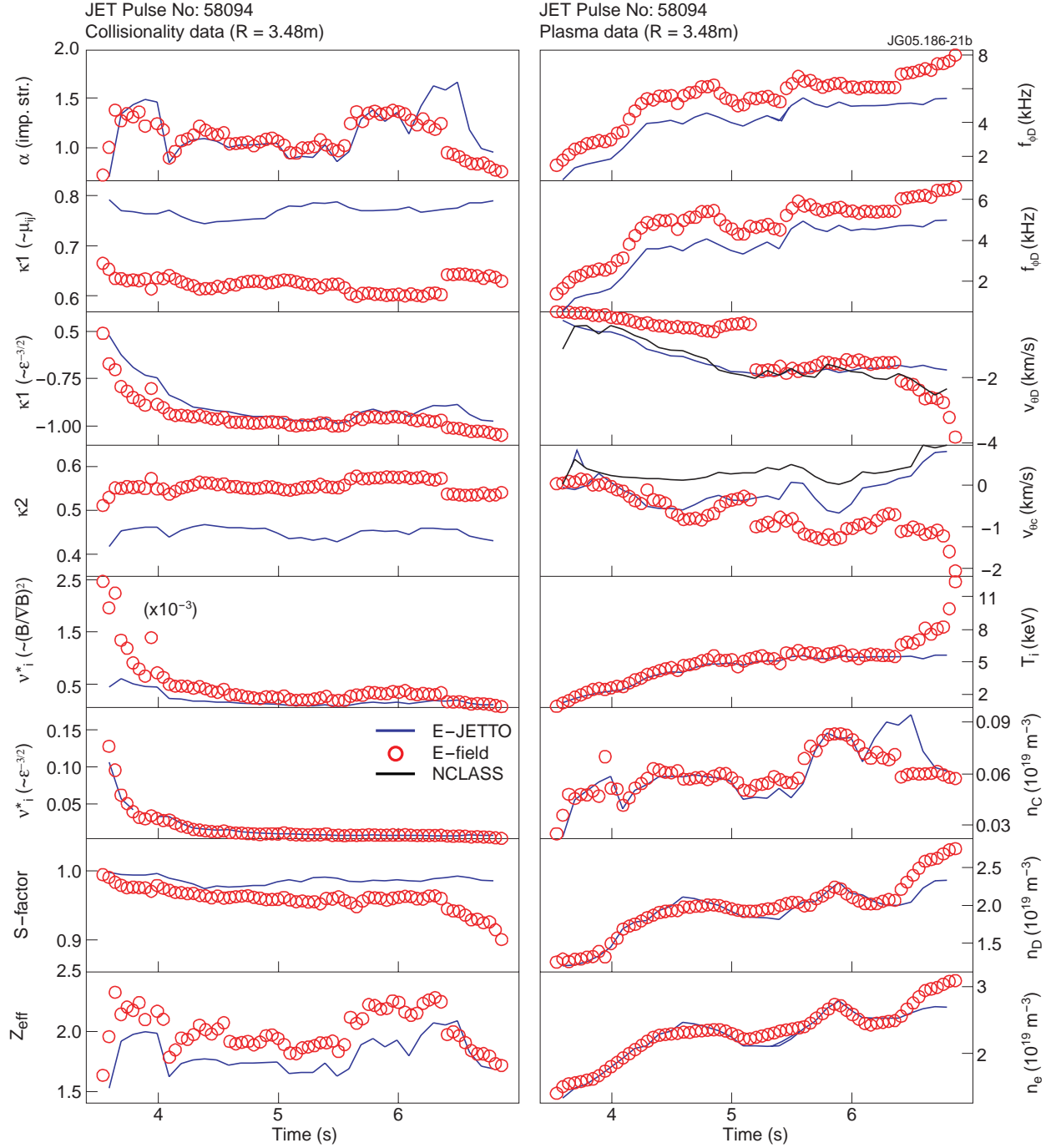
Figure 18(b): Plasma and neoclassical collisionality factors for the E_r comparison between E-field and NCLASS for the ITB Pulse No: 61349, at R=3.35m, the position of the peak $T_i(x,t)$.
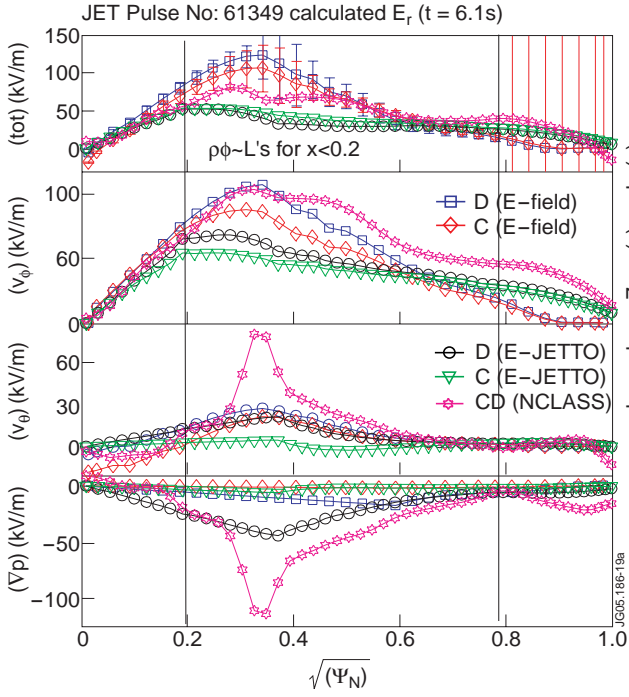
Figure 19(a): The profile of $E_r(x,t)$ and its components for Pulse No: 61349 at t=6.1sec, showing the role of potato orbits: the results are not reliable for x<0.2, since $\rho_{\theta D}(x,t)=O(L_{pD}(x,t))$, and have a very strong sensitivity on the Z_{EFF} and density profiles towards the plasma edge, for x>0.8.
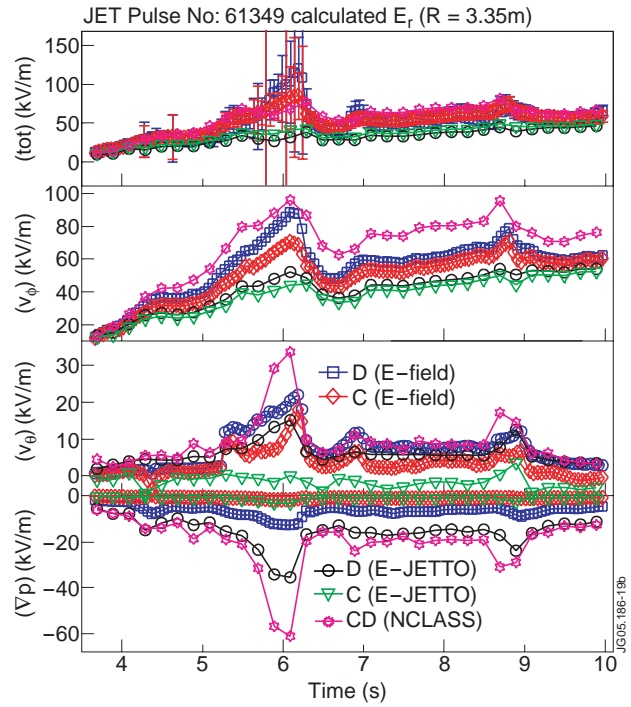
Figure 19(b): The evolution of $E_r(x,t)$ and its components at R=3.35m, around the foot of the ITB: note the slow build-up of the toroidal component due to the improved confinement.
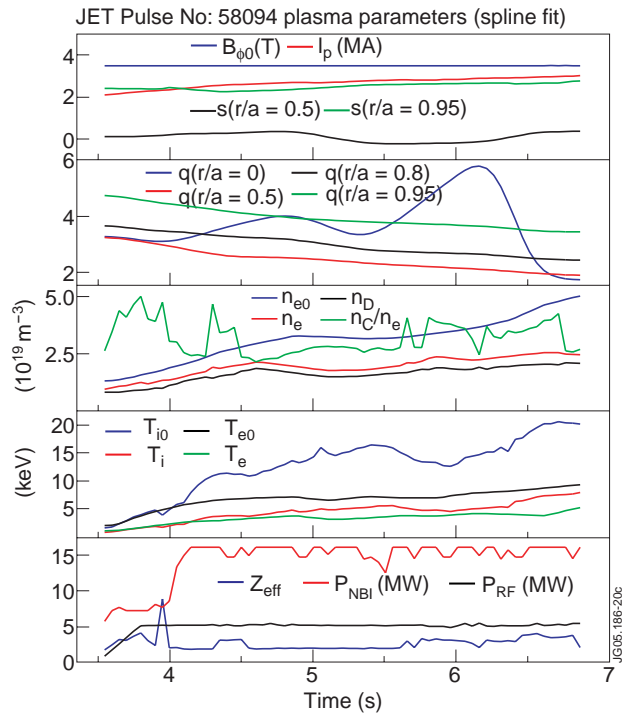
Figure 20: The main plasma parameters for Pulse No: 58094, a JET ITB pulse with a flat q-profile in the plasma core, hence smaller potato orbits that those in Pulse No: 61349.

Figure 21(a): Plasma and neoclassical collisionality factors for the E_r comparison between E-field and NCLASS for Pulse No: 58094 at t=6.6sec, during the ITB phase.

Figure 21(b): Plasma and neoclassical collisionality factors for the E_r comparison between E-field and NCLASS for Pulse No: 58094 at R=3.48m, the position of the foot of the ITB.
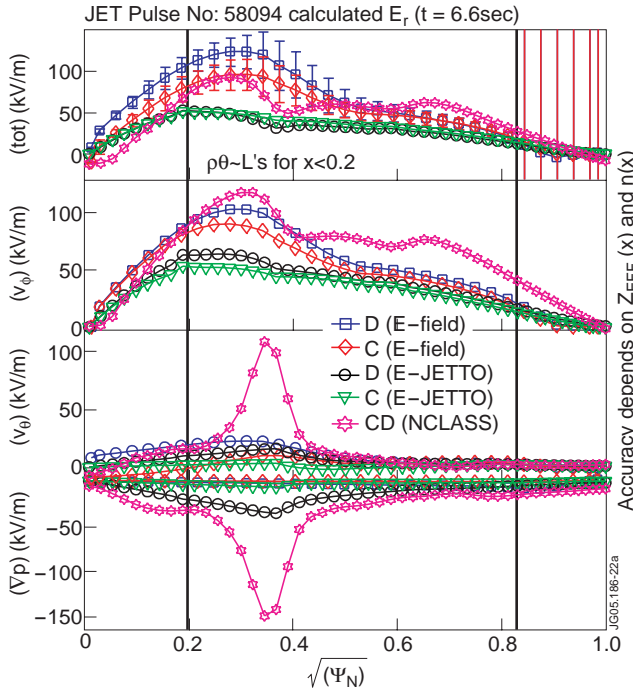
Figure 22(a): The profile of $E_r(x,t)$ and its components for Pulse No: 58094 at t=6.6sec: note again the clear smoothing of the $\nabla p/n$ and $V_\theta \times B_\phi$ components due to the averaging over the ion orbit width.
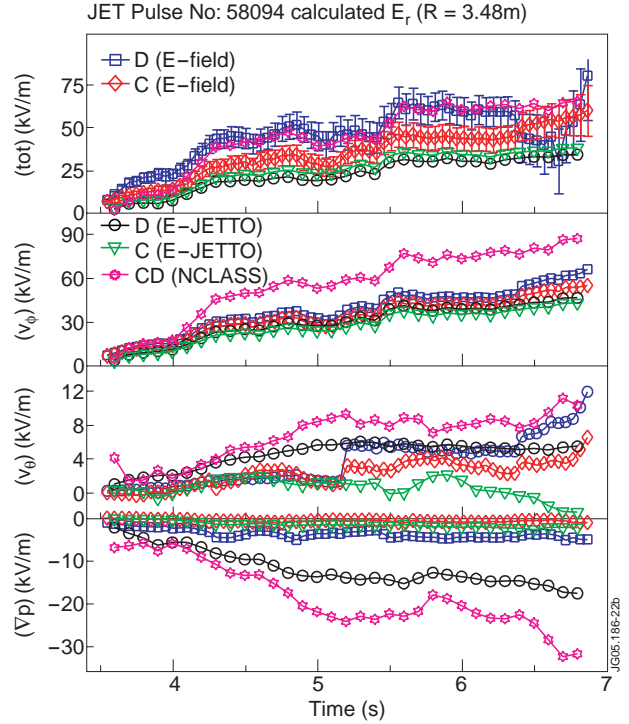
Figure 22(b): The evolution of $E_r(x,t)$ and its components at R=3.48m, around the foot of the ITB: due to the smaller ion orbit width, in this case the NCLASS and E-field calculation are much closer.
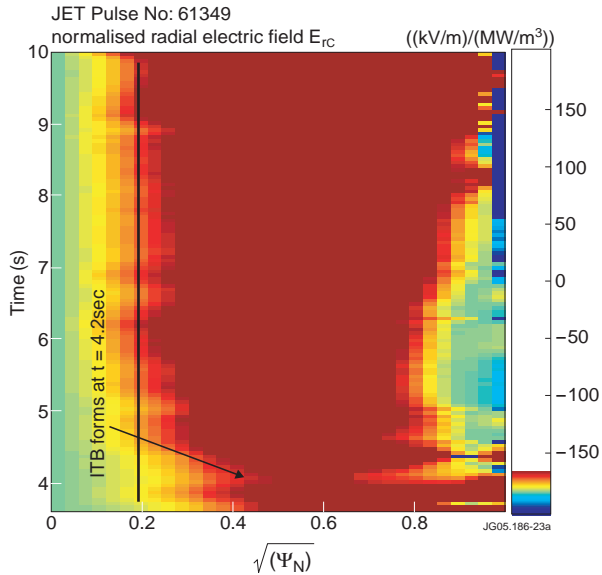

Figure 23(a): The 3D radial electric field for the ITB plasma Pulse No: 61349: note the broad profile due to the very large ion orbit width in this case, and the rapid sequence of drop/increase/broadening of E_r at the ITB onset around mid-radius.
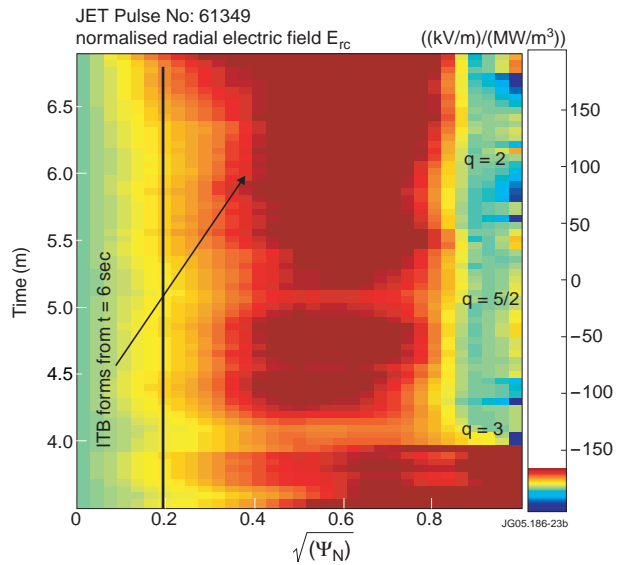

Figure 23(b): The 3D radial electric field for the ITB plasma Pulse No: 58094: here $E_r(x,t)$ is much more peaked than in the comparison Pulse No: 61349, because of the smaller potato orbits. Note as well the transient drops in $E_r(x,t)$ at thee appearance of low-order rational q-surfaces around mid-radius.
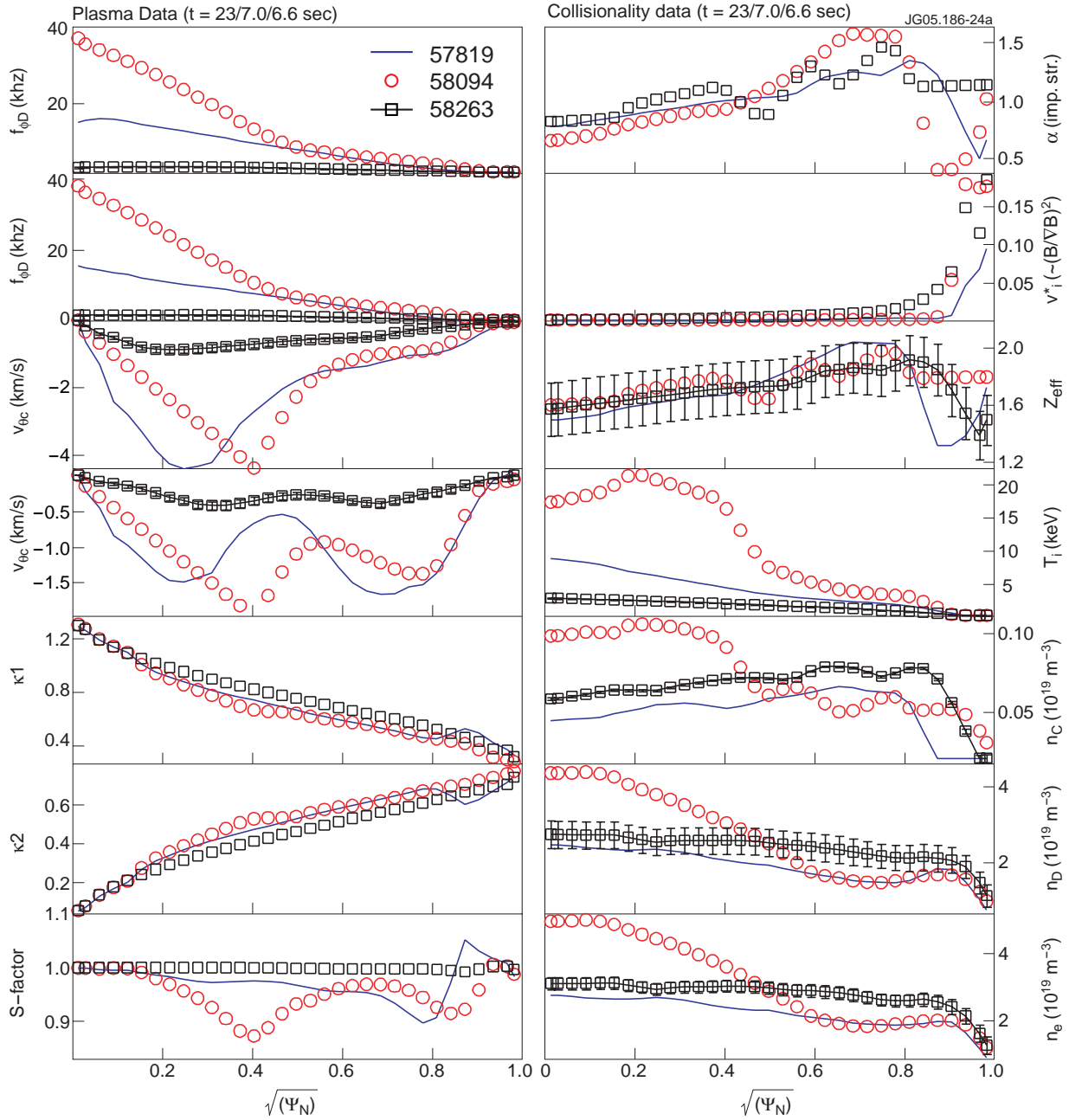
Figure 24(a): Plasma and neoclassical collisionality factors for the E_r comparison between L-mode, H-mode and ITB plasmas (small potato orbits).
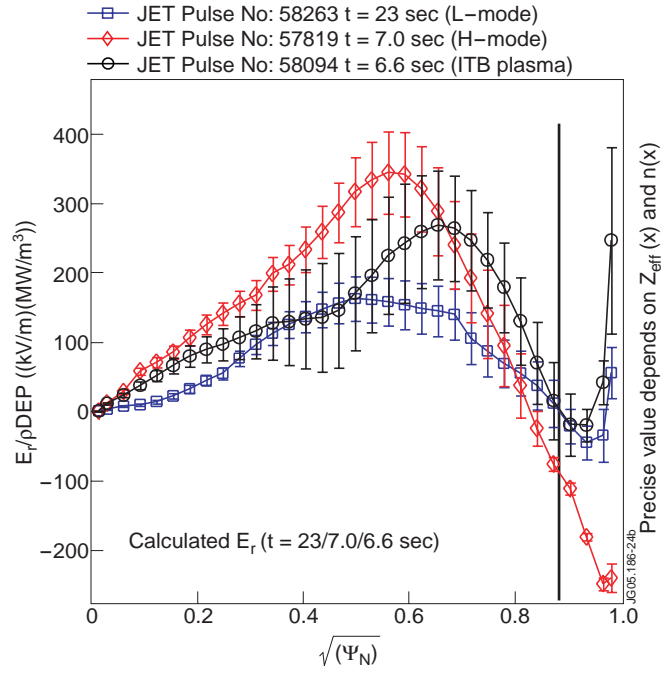
Figure 24(b): The computed $E_r(x,t)$ normalised with respect to the input power deposition profile to take empirically into account the different momentum input. Note the striking similarity in the shape of E_r/ρ_{DEP} up to around mid-radius between L-mode and ITB plasmas. The H-mode radial electric field is definitively negative for $x>0.85$, hovering around $E_r(x,t)=0$ for L-mode plasmas, and positive for ITB plasmas, although in this case there are very significant error bars.